INSTITUTO SUPERIOR DE ENGENHARIA DE LISBOA

Área Departamental de Engenharia Eletrotécnica Energia e Automação

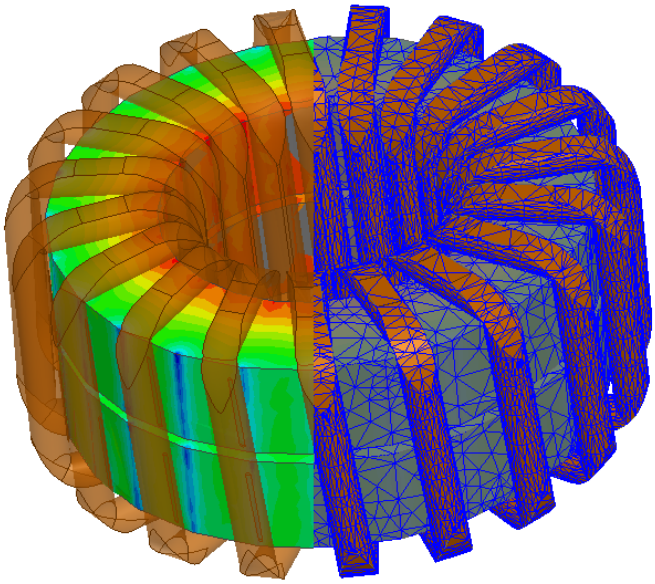

Toroid Inductor Development for a SiC DC-DC Converter up to 150kW, based on Finite Element Method

ALEXANDRE EMANUEL DA SILVA BENTO

(Licenciado em Engenharia Eletrotécnica)

Dissertação para a obtenção do grau de Mestre em Engenharia Eletrotécnica – ramo de Energia

Orientador:

Doutor Ricardo Jorge Ferreira Luís

Júri:

Presidente: Doutor João Hermínio Ninitas Lagarto

Vogais:

Doutor Ricardo Jorge Ferreira Luís

Doutor Miguel Cabral Ferreira Chaves

Setembro de 2015

ABSTRACT

In this thesis an inductor for an Electric Vehicle (EV) fast charger is designed and built. The fast charger utilizes Silicon Carbide (SiC) semiconductors enabling the system to support high currents (300 A) while switching at high frequencies (up to 100 kHz). This leads to a reduction on the required inductance value for the bidirectional DC-DC converter (BDC).

The required inductance value for the BDC is calculated from its mathematical model. This inductor is required to support a DC current of 300A with a ripple component with frequency up to 100 kHz.

A group of powder core materials with toroidal core shapes are selected as best suited for the application due to the design priorities. A multi-objective optimization approach is built based on a sensibility test conducted with electromagnetic Finite Element Method (FEM) analysis. The better configurations achieved per material are then compared, where the High Flux 26µ exceeded the other powder materials in terms of size and cost while maintaining the inductor losses at acceptable values. The winding design considers litz and solid wire, in which is concluded that for this particular application the solid wire is the best option due to lower cost.

KEYWORDS

Inductor, powder core, SiC, FEM, magnetic components, DoE, sensibility study;

RESUMO

Esta tese trata do desenvolvimento de um indutor para um carregador rápido de carros eléctricos. Este sistema de carregamento utiliza semicondutores SiC, suportando assim correntes elevadas (300A) e atingindo altas frequências de comutação (100kHz). Desta maneira consegue-se reduzir o tamanho do componente magnético.

É deduzido o modelo matemático do conversor, onde é possível calcular a indutância necessária para se respeitar os limites de operação dos semicondutores.

Os materiais do tipo núcleo de partículas (*powders*) em forma toroidal são seleccionados como os mais adequados para esta aplicação devido às suas prioridades de design. É realizada uma abordagem de otimização multiobjetiva. Esta abordagem tem por base um estudo de sensibilidade conduzido com recurso a um software que utiliza o método dos elementos finitos (FEM).

As melhores configurações por material são comparadas, onde se conclui que o material High Flux 26µ supera as outras opções em termos de tamanho e custo, mantendo um valor de perdas aceitável. O projecto de enrolamento tem em consideração condutor sólido e litz, concluindo-se que o condutor sólido era uma melhor opção devido ao seu menor custo.

PALAVRAS CHAVE

Indutor, Núcleo powder, SiC, Método dos Elementos Finitos, componente magnético, DoE, estudo de sensibilidade.

ACKNOWLEDGMENTS

This thesis counted with the guidance and support of several individuals who directly or indirectly contributed to the development of this study.

Firstly, I would like to thank my academic advisor Dr. Ricardo Luís for his guidance, availability and effort during this thesis progress.

I'm grateful to Paulo Almeida for making this project possible and for being a friend, a colleague and a teacher on the course of all the work realized.

I'd also like to thank the professors from CIPROMEC for giving me the opportunity to participate in the project of the fast charger, sharing knowledge and for making me feel welcome in their working space.

The financial support and interest shown in the fast charger prototype by the part of EVTV is greatly appreciated.

Ansys Inc. supported this thesis by providing a license for their electronic simulation package. I'm also thankful to Ignacio Tife for being my contact within Ansys Inc. making the license existence possible.

A word of thanks to my grandfather Silvestre Bento for his availability and will to help me in the process of winding the inductor.

To my colleague and friends, Sérgio André and Miguel Rhodes a thank you for your support, friendship and company during our sometimes endless work sessions.

I'll always be thankful to my parents and brothers for making me able to evolve personally and professionally, and for all their unconditional love and support. I also want to thank my spectacular girlfriend, Marisa Marques for her companionship and for consistently giving me strength and confidence to face every new challenge.

To everyone on my group of high school friends who are always my getaway from stress and problems, a big thank you and a wish of best luck for our next new stages.

I finalize my acknowledgements with a very special thank you note to my grandfather Mário Silva for everything he has given and taught me all over the years. Everything I achieve will be with a little of his help.

Alexandre Bento, September 2015

SYMBOL TABLE

Symbols

A_c	Magnetic core cross section [m^2]
A_L	Inductance Factor [$H/turn^2$]
A_{surf}	Inductors surface area [cm^2]
A_{wire}	Wire cross section [m^2]
b	Core breadth [mm]
B	Magnetic Flux Density [T]
$\mathbf{B}$	Magnetic induction vector [T]
C_{A_c}	Percentage Contribution of the core's cross section to inductor losses
C_{l_m}	Percentage Contribution of the magnetic length to inductor losses
D	Duty cycle
$\mathbf{D}$	Electric flux density vector [C/m^2]
d_{wire}	Wire diameter [m]
d_s	Strand diameter on litz wire design [mm]
$\mathbf{E}$	Electric field vector [V/m]
f	Frequency [Hz]
f_{eff}	Effective frequency [Hz]
$f_{\max}$	Maximum switching frequency of the semiconductor devices [Hz]
h	Constant per strand diameter for litz wire design [mm^{-3}]
H	Magnetic field [A/m]
$\mathbf{H}$	Magnetic field vector [A/m]
Ht	Height of the toroid core [mm]
i	Current [A]
I_{ac}	rms value of the AC component of $i(t)$ [A]
I_{dc}	rms value of the DC component of $i(t)$ [A]
i_L	Inductor current [A]
$I_{\max}$	Maximum value of current of the BDC [A]
$I_{\min}$	Minimum value of current of the BDC [A]
ID	Inner diameter of the toroid core [mm]

J	Current density [A/cm^2]
$\mathbf{J}$	Current density vector [A/cm^2]
k	Ratio between the LV and HV
L	Inductance [H]
L_{load}	Inductance on load conditions [H]
$L_{no\ load}$	Inductance at no load [H]
$L_{required}$	Inductance required for the BDC [H]
l_m	Magnetic path length [m]
l_{wire}	Wire length [m]
m	Winding number of layers
$\mathbf{M}$	Magnetization vector [A/m]
N	Number of turns
n_e	Recommended number of strands on litz wire design
n	Real number of strands on litz wire design
OD	Outer diameter of the toroid core [mm]
P_{core}	Losses in the inductor's core [W]
$P_{inductor}$	Inductor losses [W]
$P_{out\,boost}$	Output power of the BDC in boost mode [W]
$P_{out\,buck}$	Output power of the BDC in buck mode [W]
$P_{winding}$	Losses in the windings [W]
R_{dc}	DC component of the winding resistance [Ω]
R_{ac}	AC component of the winding resistance [Ω]
S_{A_c}	Score of the core's cross section on inductor losses
S_{l_m}	Score of the magnetic length on inductor losses
S_{Loss}	Loss Score of a specific core configuration
T	Period [s]
T_{amb}	Ambient temperature [^{o}C]
T_{op}	Operation temperature [^{o}C]
T_{rise}	Temperature rise [^{o}C]
t	Time [s]

V_L	Inductor Voltage [V]
V_{LV}	BDC low voltage level [V]
V_{HV}	BDC high voltage level [V]
W_L	Inductor Stored Energy [J]
∇	Mathematical operator for partial derivative
δ	Skin depth [m]
Δi_L	Inductor's ripple current [A]
ε	Electric permittivity [F/m]
ϕ	Magnetic Flux [Wb]
ρ	Electric charge volume density [C/m^3]
σ	Electric conductivity [$\Omega^{-1}.m^{-1}$]
μ	Magnetic permeability [H/m]
μ_0	Magnetic permeability of free space ($4\pi \times 10^{-7}$) [H/m]
μ_r	Relative magnetic permeability
ξ	Ratio of wire diameter to skin depth ($\times \frac{\sqrt{\pi}}{2}$)

ABBREVIATIONS

AC – Alternating current

BDC – Bidirectional dc-dc converter

DC – Direct current

DoE – Design of Experiments

EMI – Electromagnetic Interference

EV – Electric vehicle

FEA – Finite Element Analysis

FEM – Finite Element Method

FFT – Fast Fourier Transform

HV – High voltage

LV – Low voltage

MOSFET – Metal Oxide Semiconductor Field Effect Transistor

MPP – Molypermalloy powder

rms – root mean square

SiC – Silicon Carbide

VBA – Visual Basic

TABLE OF CONTENTS

LIST OF FIGURES

LIST OF TABLES

Chapter 1

Introduction

1.1 – Scope and Motivation

This thesis is part of a project developed by Instituto Superior de Engenharia de Lisboa (ISEL) in partnership with Electric Vehicle Television (EVTV). It consists in the development of a fast charger for electric vehicles applications with very specific and ambitious specifications. The thesis focuses on the design of an inductor to be used on the first prototype of the fast charger.

Power electronic systems are meant to be efficient, small and cost-effective. Magnetic devices constitute a major part of these systems. Therefore its design is of vital importance to power electronic systems performance. The big complexity involved in the design of magnetic components requires the use of computer assisted design techniques in order to predict the component behavior without investing excessive resources to build physical prototypes.

1.2 – Objectives

The principal objective of this thesis is to achieve the optimal inductor design in terms of size, robustness, cost effectiveness and efficiency for a bidirectional in current DC-DC converter. This is done recurring to Finite Element Analysis (FEA) and Design of Experiments (DoE).

In this context the main objectives of this thesis are the following:

1. Magnetic materials used in today's power electronics review;
2. Build a mathematical model of the fast charger;
3. Create a fast charger numerical simulation model to validate the mathematical model results;

4. Restrict the inductor design to the best suited materials taking into consideration the fast charger operating conditions and its design priorities;
5. Conduct a sensibility study in order to find the optimal core configuration;
6. Consider the possible winding arrangements in order to achieve the optimal inductor;
7. FEA of the final inductor where the different design technique results are compared;
8. Build the designed inductor and introduce relevant measurement techniques for its application.

1.3 – Thesis outline

This thesis is divided into six chapters, being the first and the sixth the introduction and conclusion respectively.

Chapter two summarize the main theoretical concepts of inductors for power electronics presenting the available materials and core shapes on the market.

Chapter three introduces the fast charger, where it's stated the basic power electronic converter functioning modes and its operation limits. The required inductance value is calculated from power electronic converter's mathematical model, and then the numerical simulation model of the bidirectional in current DC-DC converter is developed to analyze its charging and discharging operation modes.

Chapter four emphasizes the inductor design, which includes a sensibility study of the core dimensions effect on the inductor losses, creation of a ranking of configurations based on the sensibility study, FEA of the best ranked configurations, winding design in which litz and solid wire are considered, and finally a confirmation that the operating temperature is within the material limits.

Chapter five consists of documenting the process of building the inductor and treats the topics on how to measure experimentally the inductance and power losses of the component.

1.4 – Numerical simulation and development tools

The work developed during this thesis required the usage of different simulation tools and scripts.

On Chapter 3 the fast charger's numerical simulation model has been implemented on Matlab/Simulink from MathWorks. This software features a set of libraries with functions to solve particular problems. This model utilized the library SimPowerSystems and the tool FFT (from Fast Fourier Transform).

The FEA has been performed on Ansys Maxwell. This software applies Finite Element Method (FEM) to solve electric and magnetic problems. It contains seven different solvers, each for a specific type of electromagnetic problem. These are: Magnetostatic, Eddy Currents solver, Transient Magnetic, Electrostatic, DC conduction, AC conduction (2D problems) and Transient Electric [1].

Visual Basic (VBA) scripts have been implemented in Microsoft Office Excel Macro in order to do repetitive calculations automatically.

Chapter 2

Inductors for Power Electronics

2.1 – Introduction

Power electronics is a growing field, which tends to develop smaller, more robust, with higher efficiency and more potent systems. Nowadays the semiconductors can support high currents and high switching frequencies with good efficiency. Magnetic components are required to be more efficient and compact in size while subjected to higher electrical transient inputs. This forces the inductor design to be more meticulous.

The innovation on the inductors field is made creating new alloys from mixing different elements in different quantities, developing better processes of fabrication of these alloys which in some cases have big impact on the final material magnetic properties [2][3].

In this chapter important theoretical concepts that are part of inductor design are reviewed. Also the most common core materials and shapes existent in the magnetic components market are introduced.

2.2 – Theoretical concepts of inductors

Inductors are magnetic components, its design require the knowledge of some challenging concepts of magnetic fields and energy.

2.2.1 – Inductance

Inductance is the capability of storing energy in form of magnetic flux of an inductor. It depends on the geometrical dimensions of the core and its material properties.

The derivations presented in this subsection are taken from [4]. An inductor is composed winding made of an electrical conductor material around a core, which is made of a soft magnetic material.

Michael Faraday, in 1831 discovered that a varying magnetic flux passing through a winding would induce a voltage. This relation is described by one of the Maxwell equations and is known as the Faraday's law, given by (2.1). Where N is the coil number of turns and ϕ is the magnetic flux passing through each turn of the coil.

$$V_L = N\frac{d\phi}{dt} \tag{2.1}$$

From electrical circuit theory, the inductor voltage, V_L, created by a current, i, flowing through the inductor winding, with inductance L, is given by (2.2).

$$V_L = L\frac{di}{dt} \tag{2.2}$$

Setting (2.2) and (2.1) equal to each other, integrating is respect to time to remove the differential operators, and solving for the inductance. It's obtained (2.3), which establishes a relation between electric and magnetic field quantities.

$$L = \frac{N\phi}{i} \tag{2.3}$$

A magnetic flux passing through an area, A, is the integral of the magnetic flux density (also called magnetic induction), B, over that area.

$$\phi = \int B\,dA \tag{2.4}$$

In the case of uniform flux density and no air gap, (2.4) becomes (2.5).

$$\phi = BA \tag{2.5}$$

The magnetic flux density, B, and the magnetic field, H, are related by (2.6). Where μ_0 is the magnetic permeability of the vacuum and μ_r is the relative permeability of the material.

$$B = \mu_0\mu_r H \tag{2.6}$$

Ampere law states that the integral of the magnetic field along a closed path is proportional to the current flowing through the coil multiplied by its number of turns, as stated on (2.7).

$$\int H\,dl = Ni \tag{2.7}$$

If the coil is extended around into a toroidal shape, the magnitude of the magnetic field will be essentially constant inside the toroid. Ampere's law applied to the toroid becomes (2.8).

$$Hl = Ni \tag{2.8}$$

Grouping everything and returning to (2.3), it's obtained the expression for inductance (2.9), valid under the assumptions stated above, where A_c is the core cross section and l_m is the length of the magnetic path.

$$L = N^2 \mu_0 \mu_r \frac{A_c}{l_m} \tag{2.9}$$

Magnetic core material manufacturers for each specific core give the value of the inductance factor, A_L. This factor is called core's permeance and corresponds to the inverse of the core's magnetic reluctance. The no-load inductance is obtained by (2.10).

$$L = N^2 A_L \tag{2.10}$$

Also important is the definition of stored energy of the inductor, W_L, which considering the magnetic circuit linear is calculated using (2.11).

$$W_L = \frac{1}{2} L i^2 \tag{2.11}$$

2.2.2 – Magnetization curve and Hysteresis loop

The magnetization curve, also called the B-H curve relates the magnetic flux density to the magnetic field in a material. There are three types of materials:

- Diamagnetic materials
- Paramagnetic materials
- Ferromagnetic materials

Diamagnetic materials have a value of relative permeability close but less than unity, this means that they exclude the magnetic field. Examples of diamagnetic materials are copper, silver and gold. Superconductors are a specific class of diamagnetic materials [5].

Paramagnetic materials have a relative permeability slightly bigger than unity. This means that they are slightly magnetized when a magnetic field is applied. Examples of paramagnetic materials are aluminum, platinum and manganese.

Ferromagnetic materials are characterized by very high values of relative permeability (10-100.000) [5]. These are the materials that are used in power electronic magnetic components and some of these materials will be introduced later in this work.

Figure 2.1 presents the comparison of the B-H relation for different type of magnetic materials. It is possible to see that ferromagnetic materials have a linear characteristic for a part of the curve, but at certain point they show a nonlinear magnetic characteristic, which results in a varying magnetic permeability. This happens because the ferromagnetic material starts to saturate.

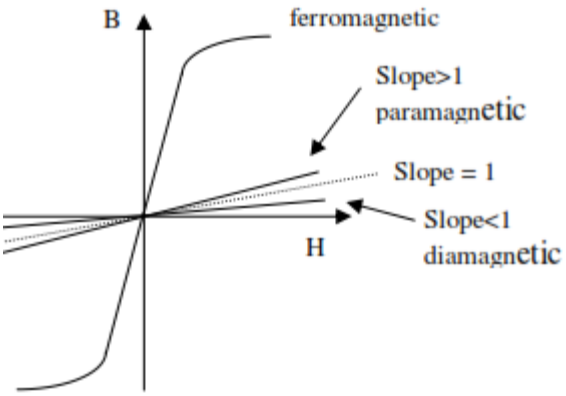

Figure 2.1- Magnetization curves for different types of magnetic materials.

The magnetization curve only happens on the first magnetization of the material, after that a hysteresis loop will take place. This loop represents the magnetic behavior of a material. The losses in the material due to hysteresis are obtained calculating the area of the hysteresis loop. Figure 2.2 shows a typical hysteresis loop of a ferromagnetic material. There are three important points in the loop, each one with a symmetric point, they are:

- Saturation;
- Residual Magnetism;
- Coercive force

Saturation flux is the point where the maximum flux density supported by the material is reached.

Residual magnetism is the flux density that the material saves when the applied magnetic field intensity is reduced to zero.

Coercive force is the magnetic field that needs to be applied in opposite direction of the flux density in order to bring the flux density back to zero.

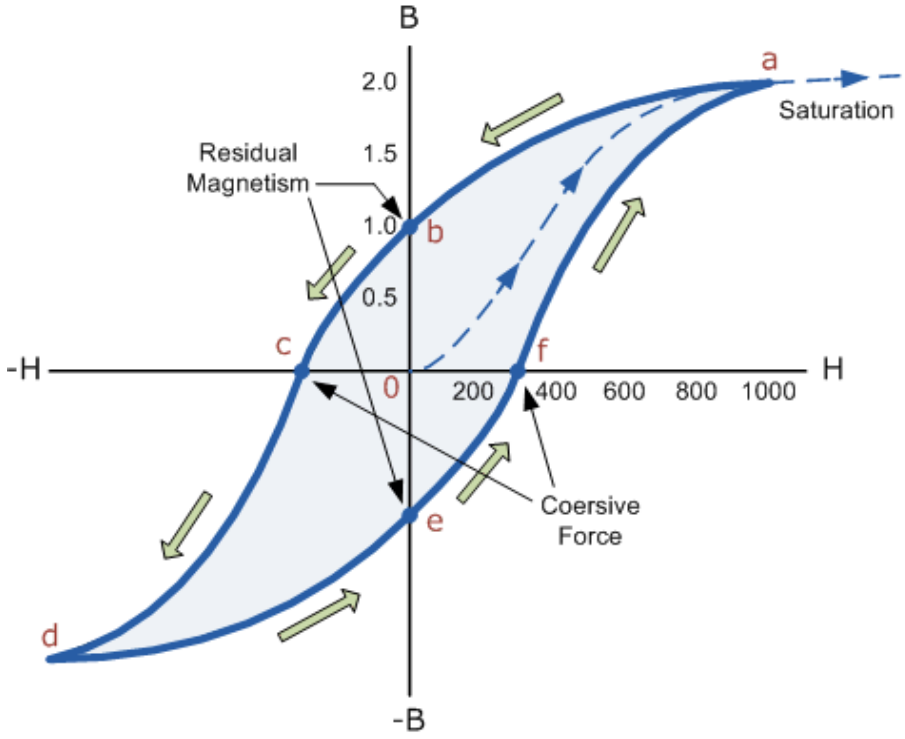

Figure 2.2 – Typical hysteresis loop of a ferromagnetic material.

Ferromagnetic materials are subdivided in two classes, according to its coercive force, they are:

- Soft magnetic materials;
- Hard magnetic materials.

Soft magnetic materials are characterized by a small coercive force and a narrow hysteresis loop. Most of the magnetic components use cores made from soft magnetic materials.

Hard magnetic materials are characterized by strongly resisting the influence of an external magnetic field. This is seen on the hysteresis loop by a very strong coercive force. They are used as permanent magnets and one of its most important characteristics as magnets is the residual induction. Figure 2.3 shows the differences from the two types of ferromagnetic materials.

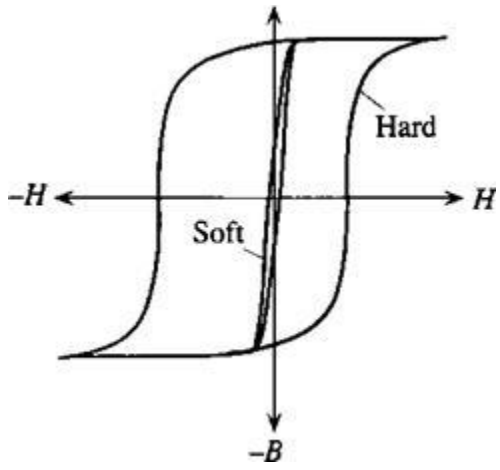

Figure 2.3 – Soft vs Hard magnetic material hysteresis loop.

2.2.3 – Eddy currents

From Faraday's law (2.1), a time varying magnetic flux will induce a voltage which origins a current. In an inductor, both the core and the winding are subjected to time varying fields. This will induce eddy currents that will flow through the core and the winding producing resistive losses. These currents will depend on the resistivity of the material, on the frequency and on the magnitude of the varying magnetic flux.

In gapped cores winding and gap design needs special consideration on the gap region, especially on high frequency applications, this is because the magnetic flux in the gap spreads to a bigger area than the core's cross section, see Figure 2.4, the phenomenon of spreading the flux is called fringing flux [6]. Windings in the fringing region are induced with eddy currents that may result in big additional losses. Therefore ways of optimizing the copper arrangement and disposition near gap regions are employed on power electronic applications [7][8].

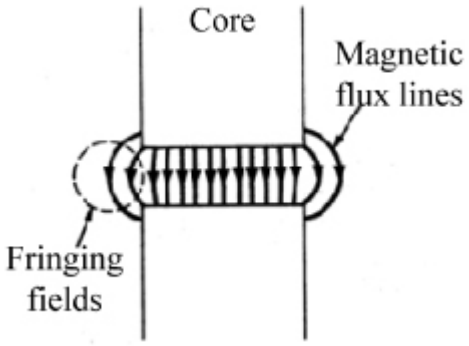

Figure 2.4 – Fringing flux illustration.

2.2.4 – Skin and Proximity effects

Direct consequences of eddy currents are skin and proximity effects.

Skin effect

A DC current flowing through a conductor wire distributes itself uniformly on the conductor maintaining the current density, J , constant on the wire's cross section. An AC current will produce time varying magnetic fields. With the increase in frequency, the fields get stronger and the flowing electrons are pushed to the conductor's surface, forcing the current density to be bigger on the conductor surface and smaller on its center, this is called Skin effect and causes an increase in the wire resistance for the AC component of the current. In order to understand clearly the skin effect, the concept of skin depth, δ , must be introduced. Skin depth is defined as the distance from the conductor surface to where the current density (inside the wire) is attenuated to 1/e from the current density observed on the surface [9]. Skin depth is given in meters and it's calculated by (2.12), where σ is the electrical conductivity of the wire material and μ is its magnetic permeability.

$$\delta = \sqrt{\frac{1}{\pi f \mu \sigma}} \tag{2.12}$$

Proximity effect

Another important phenomenon in inductors is the proximity effect, this happens because the conductors are usually close to each other. A varying current flowing through the wires produces magnetic fields that induce the adjacent wires interfering with their current density. Proximity effect also increases with the rise in frequency, augmenting the AC resistance.

Figure 2.5 illustrates the origins and the consequences of skin and proximity effects.

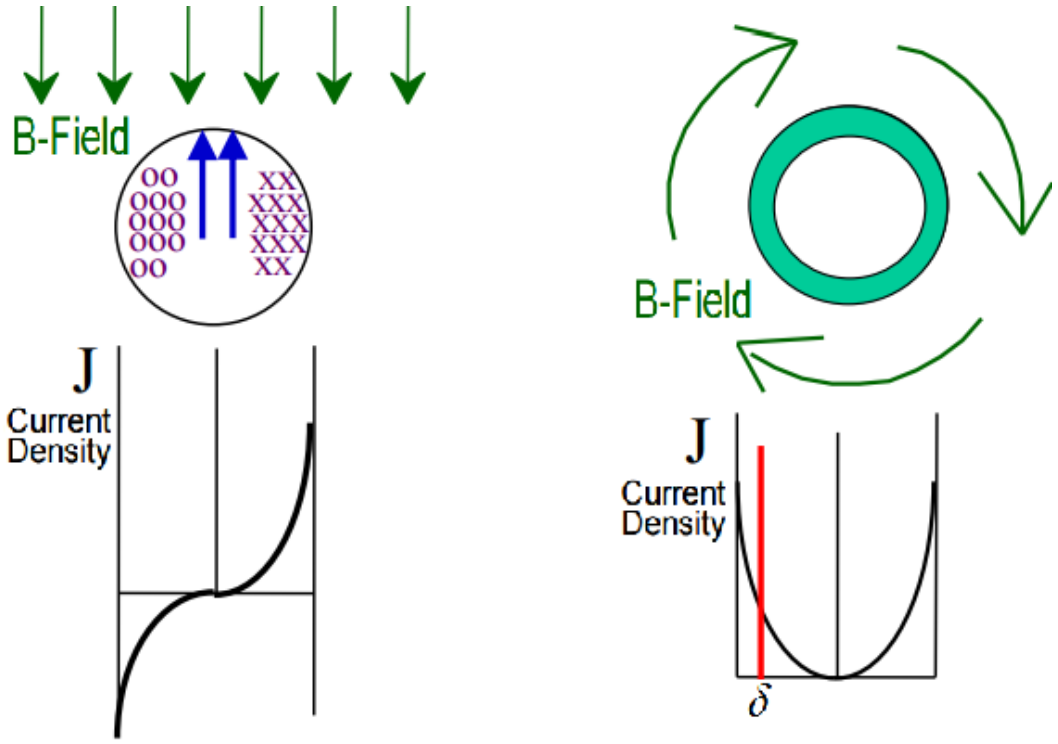

(a) (b)

Figure 2.5 – Illustration of eddy current effects on conductors: (a) proximity effect, (b) skin effect.

In inductor design literature, these effects are usually approached together. This is done by calculating the ratio of AC resistance, R_{ac} , to DC resistance, R_{dc}. For a solid round wire, the ratio of AC to DC resistance is calculated by (2.13), where m is the number of wire layers of the inductor and ξ represents a ratio between the wire diameter and the skin depth for the specified frequency. This ratio is obtained from (2.14), where d_{wire} is the diameter of the solid conductor [10][11][12].

$$\frac{R_{ac}}{R_{dc}} = \frac{\xi}{2}\left[\frac{\sinh(\xi)+\sin(\xi)}{\cosh(\xi)-\cos(\xi)} + (2m-1)^2 \frac{\sinh(\xi)-\sin(\xi)}{\cosh(\xi)+\cos(\xi)}\right] \tag{2.13}$$

$$\xi = \frac{\sqrt{\pi}}{2}\frac{d_{wire}}{\delta} \tag{2.14}$$

The winding losses due to the AC component of the inductor current are calculated by (2.15). If the AC component isn't sinusoidal the AC component current can be decomposed on series of Fourier and the calculations (2.13) and (2.15) are repeated for each harmonic frequency

taken into account. The AC losses is the sum of the losses due to each harmonic [11]. Note that the current used to calculate resistive losses is the root mean square (rms) value. The DC resistance is obtained by (2.16), where l_{wire} is the length of the wire and A_{wire} is the wire cross section.

$$P_{ac} = R_{ac} I_{ac}^2 \tag{2.15}$$

$$R_{dc} = \frac{l_{wire}}{\sigma A_{wire}} \tag{2.16}$$

2.3 – Losses in Inductors

Both the winding and the core of the inductor have losses. These losses depend on several factors (*e.g.* application, frequency, materials, temperature, *etc.*). This section presents ways of predicting the losses in power inductors.

2.3.1 – Winding Losses

Losses in windings are due to DC and AC components of the conductor resistance, these two components were discussed in detail in Section 2.2.4 where the skin and proximity effects were explained. The total losses in the inductor windings are obtained by (2.17), where n is the nth harmonic from the AC current decomposition into a Fourier series [11].

$$P_{winding} = R_{dc} I_{dc}^2 + \sum_{n=1}^{\infty} R_{ac_n} I_{ac_n}^2 \tag{2.17}$$

When the losses due to the increased AC resistance are high, different windings types such as multistrand, foil and litz wire with conductor diameter near skin depth are used[10].

2.3.2 – Core Losses

According to [5] and [13] the total core loss can be decomposed into a sum of three components:

- Hysteresis losses;

- Eddy Current losses;
- Anomalous Losses.

In order to magnetize a material, a magnetic field is applied, which aligns its magnetic domains and creates a magnetic flux, this consumes energy. If the magnetic field applied is of sinusoidal excitation, the hysteresis loop will be contoured one time per cycle of the excitation. This means that the energy spent to magnetize a material with sinusoidal excitation is directly dependent on the frequency of the excitation field and on the area of the hysteresis loop. The energy spent per second magnetizing the material is called Hysteresis losses.

Eddy current losses, as stated in Section 2.2.3 are associated with the variation of magnetic flux that induces currents on the core material. All magnetic materials have some electrical conductivity, principally the iron-based materials which have a relatively high conductivity. The currents induced are proportional to the variation of the magnetic flux which means that the losses per eddy currents grow with the increase of the variation of the magnetic flux applied.

Under AC measurement conditions, there are extra losses that aren't explained by any of the two phenomenon stated above, these extra losses are called anomalous losses and they are attributed to different mechanisms in the magnetization process [5].

A much more analytic and complete approach to core losses calculation is presented in [5], in this thesis a more practical approach is looked for. Core manufacturers in their catalogue give curves for each material. These curves are taken from data obtained on lab measurements under sinusoidal excitation and fitted to the original Steinmetz equation [14]. The engineer just need to know the conditions in which the inductor will be functioning in order to obtain the specific loss, this is the loss per unit of volume, for each material.

2.4 – Core Materials

The magnetic components market offer lots of options when it comes to core materials, the best choice for a specific design depends on its requirements and trade-offs between size, efficiency, weight, operating temperature and frequency [12]. The inductor performance and size are strongly dependent on the operating current, current ripple, operating frequency and air gap length [15].

According to [5] there are two basic classes of soft magnetic materials:

1. Iron based soft magnetic materials which are usually called ferromagnetic materials. They are alloys of iron which contain some amounts of other elements such as Silicon (Si), Nickel (Ni), Chrome (Cr) and Cobalt (Co). In power electronics this class is divided into 3 different categories of materials:
    a) Powder Cores
    b) Amorphous Alloys
    c) Nanocrystalline magnetic materials
2. Ferrites are usually called ferrimagnetic materials. They are ceramic materials, basically mixtures of oxide of iron and other materials such as Manganese (Mn), Zinc (Zn), Nickel (Ni) and Cobalt (Co). They are characterized by a very high electrical resistivity. When compared to ferromagnetic materials, ferrites resistivity is at least one million times higher.

2.4.1 – Powder cores

This category of materials is composed by different alloys of ferromagnetic materials that are made into powder. For simple iron powder cores the resulting dust is bonded with an organic electrically non-conductor material making the final core subject to thermal aging under high temperatures [16]. In more noble alloys of powder core materials, such as Molypermalloy powder (MPP), High Flux and Kool Mu, the manufacturing process is to press the powder in the presence of a non-organic binder, eliminating the thermal aging effect. The pressed powder core alloys have significant lower core losses than the powdered iron cores. The power loss of is related to the particle size as the finer the grain the lower the losses, but higher the manufacturing cost. The permeability of the core depend on the alloy content, particle type and size, bonding material, applied pressure, heat treatment, *etc.* [17].

An important characteristic of these materials is its distributed air gap, instead of the usual discrete air gap, this brings many advantages such as soft saturation, low EMI (Electromagnetic interference) due to reduction of flux leakage and fringing flux, and low acoustic noise level [18].

The thesis aims to design an inductor for a specific application, its specifications, which are introduced on Chapter 3, fit on the powder materials "preferred zone" of operation. For this reason a more detailed presentation on the powder core materials existent on the market is done.

Iron Powder

This is the cheapest of the powder materials. It's obtained directly from iron with low carbon content which results in a high saturation flux (between 1-1.5 T). Its disadvantages compared to the other powder materials are high core loss and to be subjected to thermal aging effect due to the organic binder used in its manufacturing process.

MPP

This is the most expensive of the powder materials. It's made from an 81% nickel, 17% iron and 2% molybdenum alloy. It's the powder material with the lowest core losses and the best temperature stability. MPP saturates at 0.8 T, and exist in the market with relative permeability is in a range between 14-550.

High Flux

Composed by 50% of iron and 50% of nickel, High flux has a medium price and medium core losses. It saturates at 1.4 T and appears on the market with relative permeability in the range 14-160. It's the powder material with the best DC bias characteristic for high power density applications.

Kool Mu

This material is also known as Sendust and is made with 85% of iron, 9% silicon and 6% of aluminum [16]. It has low core losses and can be bought at low prices. It saturates around 1 T and can be obtained with relative permeability in the range 26-125.

2.4.2 – Amorphous Alloys

Also known as metallic glass, these materials are alloys of iron and other metals such as cobalt, nickel, boron, silicon, niobium and manganese. The most popular alloys are VITROVAC and METGLAS. These materials have a saturation induction between 0.7-1.8 T and an electrical resistivity 15 to 25 times higher than iron. This makes them suitable for high frequency, some alloys can be used with frequencies above 1 MHz. Amorphous alloys appear

with very high DC permeability, for example alloy 2826MB METGLAS exhibit a DC relative permeability up to 800,000 [5].

2.4.3 – Nanocrystalline

Nanocrystalline is the most recent of the soft magnetic materials categories. Its first report with excellent magnetic properties dates 1988, invented by Yoshizawa from Hitachi Metals Laboratory. It was composed by a mixture of small amounts of copper and niob into a standard alloy of iron, silicon and boron [19]. It's called Nanocrystalline because of its grain size (between 10-100 nm). These materials exhibit a linear hysteresis loop with coercivities smaller than 2 A/m and reach saturation in a range between 1.2-1.5 T, its initial relative permeability is adjustable in the range 15,000-150,000 [5].

2.4.4 – Ferrites

Ferrites are the soft magnetic material most used in the power electronics industry [5][19]. The frequency range that ferrites are used is very wide, from the kHz to GHz due to its very high electrical resistivity which contributes to very low core losses due to eddy currents. A drawback of ferrites is its low saturation induction which is in the range 0.25-0.45 T. Its initial relative permeability is in the range of 100-20,000.

The main characteristics of each group of core materials are now shown:

Table 2.1- Main core materials characteristics.

Class	Materials	B_{sat} [T]	Losses	Cost
Ferrites	W, J, T, F, etc.	0,25 – 0,45	Low	Low
Powders	High Flux, MPP, Kool Mu	0,8 – 1,4	Moderate	Medium
Amorphous	METGLAS	0,7 – 1,8	Low	High
Nanocrystalline	FINEMET	1,2 – 1,5	Very low	High

2.5 – Core Shapes

The shape of the core affects the inductor performance, this is shown on Section 2.2.1 where it's concluded that geometric parameters have effect on the inductance. Also, inductors are designed for different applications with different requirements (*e.g.* small size, large window areas to fit copper, efficiency, *etc.*), for these reasons it's more than reasonable to have different core shapes.

The basic core shapes are: toroidal core, "C" core, "E" core and Pot core.

Figure 2.6 shows the different shapes of the cores and it's been taken from [20]. On Table 2.2 a comparison between the different geometries is done [21].

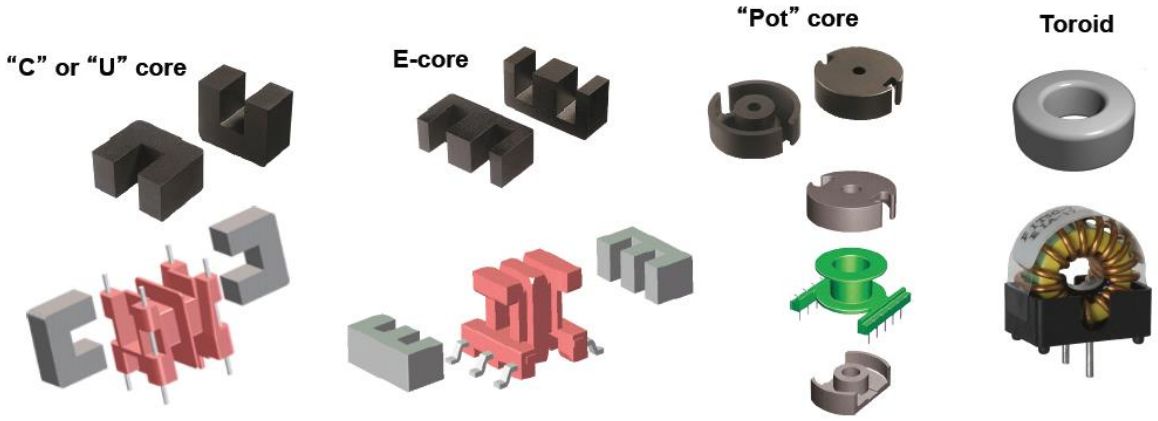

Figure 2.6 – Basic core shapes found in the market.

Table 2.2 – Comparison of different core geometries.

	Toroidal	"E" core	Pot core
Core cost	Very low	Low	High
Bobbin cost	None	Low	Low
Winding cost	High	Low	Low
Winding flexibility	Fair	Excellent	Good
Assembly	None	Simple	Simple
Mounting flexibility	Poor	Good	Good
Heat dissipation	Good	Excellent	Poor
Shielding	good	poor	excellent

As seen before, there are lots of materials that can be used as the core of an inductor. Each has its own fabrication method, which lead to some restrictions on the core shape for some materials. This is why some materials appear only in a few shapes, an example of this are some powder core materials that only exist in toroidal shape.

2.6 – Windings

The winding in high frequency and current ripple applications may be the most important part of the inductor design. This is because of losses due to the skin and proximity effect, both introduced previously.

There are three main types of windings. Those are foil, solid and litz wire. These three types are shown on Figure 2.7.

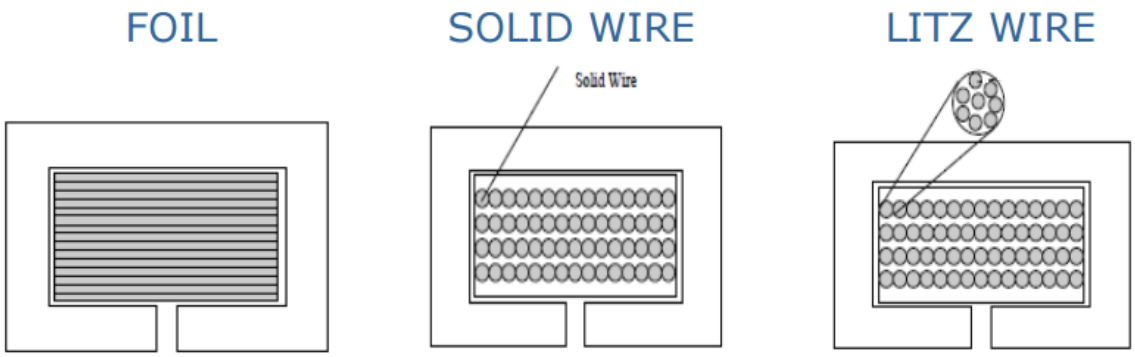

Figure 2.7 – Different types of windings.

2.7 – Conclusions

In inductor design there are lots of core material options available for the engineer, the best choice results from the priorities of the design. Each core material has its own advantages and disadvantages, some have lower core loss, and others have high manufacturing costs or support higher values of flux without saturating which contributes to lighter and smaller inductors. Efficiency and power density are very important requirements of the today's power electronics applications [22].

Chapter 3

Bidirectional in current DC-DC converter

3.1 – Introducing the converter

Bidirectional DC-DC converters (BDC) can be classified as non-isolated or isolated. Non-isolated BDCs are simpler, cheaper and more efficient than isolated BDCs [23]. For EV high power applications isolation is not usually required. There are different topologies of non-isolated BDCs. On [24] some of these topologies are introduced.

The efficiency of the BDC may be increased by employing soft switching techniques, which adds extra complexity, components and cost to the system [17].

The objective of the BDC used in this thesis is to transfer energy bidirectionally between two battery banks with different voltages. When the energy is flowing from the high voltage bank to the low voltage, the converter is functioning in buck mode. When the energy is flowing from the low voltage to the high voltage bank, the converter is functioning in boost mode.

The topology used in this work is a buck-boost non-isolated BDC, illustrated in Figure 3.1. Where V_{HV} is the voltage on the High voltage (HV) battery bank, V_{LV} is the voltage on the Low voltage (LV) side, Q_1 and Q_2 are semiconductor devices that are treated as ideal switches in the analytic analysis. In this thesis work the High and Low voltages are imposed by the battery banks, so the only thing possible of controlling is the charging power by adjusting the DC current of the inductor. This is done with a hysteretic controller that limits the current to a maximum and minimum value. The difference between these two values is called the current ripple.

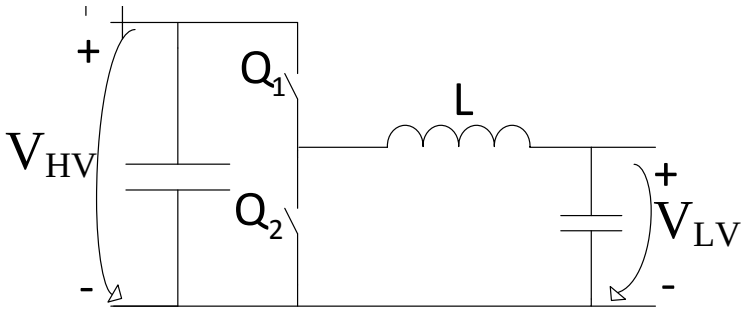

Figure 3.1 – Non-isolated BDC topology.

3.1.1 – Buck mode

In this mode the power is flowing from the HV to the LV bus. The inductor current is controlled by combining the stages of Q_1 and Q_2.

Table 3.1 – BDC Buck mode basic functioning.

i_L value	Switches state		Current path
$i_L \leq I_{min}$	Q_1	ON	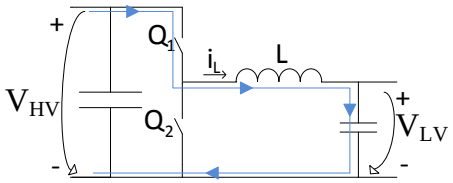
	Q_2	OFF	
$i_L \geq I_{max}$	Q_1	OFF	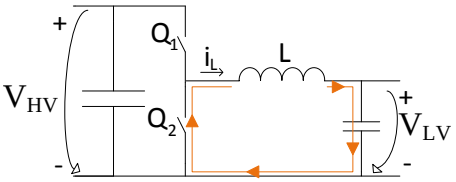
	Q_2	ON	

Analyzing the two stages of BDC functioning, it's possible to observe that the first stage (with blue color) makes the current rise at a ratio defined by the difference from the HV bus to the LV bus, but also by the value of the inductance. On the second stage (with orange color) the current doesn't invert the polarity because the inductor has magnetic energy stored, this forces the current to not vary abruptly, and making it decrease at a ratio defined by the LV voltage and the inductance value. The current in the inductor is shown in Figure 3.2, the change from

stage one to two happens on instant DT, where D is the duty cycle and T is the period of the current wave. On instant T the current reaches its minimum value and it's time to change the state of the switches again.

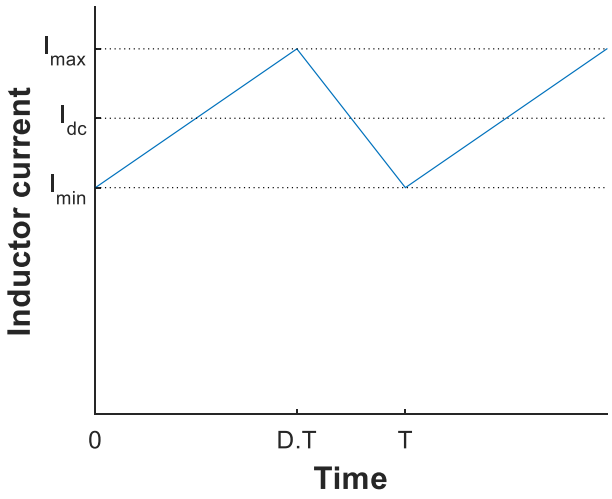

Figure 3.2 – Typical inductor current wave on Buck-Boost converter.

3.1.2 – Boost mode

The boost mode is much similar to the buck, but with the current flowing on the opposite direction. On the first stage (green color) the current is forced to flow on the circuit without the HV bus in order to make the current rise. When the current is at the maximum value, the switch Q_2 is turned OFF, and the switch Q_1 is turned ON making the current flow through the HV bus, this is stage two. In this stage the current value starts to decrease, when it reaches the minimum value of current, it's time to change to the first stage again.

Table 3.2 – BDC boost mode basic functioning.

i_L value	Switches state		Current path
$i_L \leq I_{min}$	Q_1	OFF	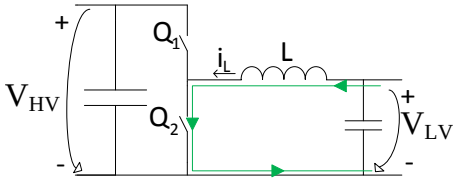
	Q_2	ON	
$i_L \geq I_{max}$	Q_1	ON	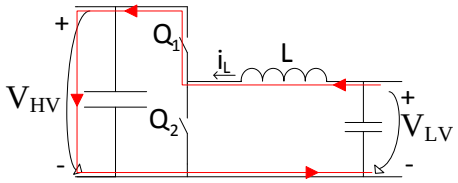
	Q_2	OFF	

3.1.3 – Mathematical model

Buck

Each stage of the buck mode has one dynamic equation. For ease of understand lets introduce basic relations, where k is the ratio between the LV and the HV ($k \leq 1$), T is the current wave period, D is the duty cycle and f is the frequency.

$$V_{LV} = kV_{HV} \tag{3.1}$$

$$DT = \frac{D}{f} \tag{3.2}$$

$$T - DT = \frac{1-D}{f} \tag{3.3}$$

Assuming that the current varies linearly, the following assumption can be made:

$$V_L = L\frac{di_L}{dt} \approx L\frac{\Delta i_L}{\Delta t} \tag{3.4}$$

The following system of equations is obtained:

$$\begin{cases} V_{HV} = V_L + V_{LV} \\ V_L = V_{LV} \end{cases} \Rightarrow \begin{cases} L\dfrac{\Delta i_L\, f}{D} = V_{HV}\left(1-k\right) & ,0 \le t \le DT \\ L\dfrac{\Delta i_L\, f}{\left(1-D\right)} = k V_{HV} & ,DT \le t \le T \end{cases} \tag{3.5}$$

Setting V_{HV} of the 1st equation equal to the V_{HV} of the second, it's possible to find the relation between the duty cycle and the ratio of the voltages in buck mode:

$$D = k \tag{3.6}$$

This means that the ratio of the period that switch Q_1 is ON is equal to the ratio of the LV by the HV.

The switching frequency of the converter depends on the input voltages and the inductance of the system. Since the inductance will be fixed, it's important to know in which conditions of input voltages the maximum frequency is reached. This is obtained by using one of the equations from (3.5), solving for f, then deriving it in order to k and setting the derivative equal to zero. This is done in (3.7), and it's concluded that the maximum frequency happens when the LV is half of the HV.

$$\frac{df}{dk} = 0 \quad \Rightarrow \quad k = \frac{1}{2} \tag{3.7}$$

The output power on buck mode is calculated by (3.8), where $i_{L\,avg}$ is the average value of the inductor current.

$$P_{out\ buck} = V_{LV} i_{L\,avg} \tag{3.8}$$

Boost

In the boost mode, the relationships stated before are maintained. The following system of equations is obtained:

$$\begin{cases} V_L = V_{LV} \\ V_{HV} = V_L + V_{LV} \end{cases} \Rightarrow \begin{cases} L\dfrac{\Delta i_L\, f}{D} = k V_{HV} & ,0 \le t \le DT \\ L\dfrac{\Delta i_L\, f}{\left(1-D\right)} = V_{HV}\left(1-k\right) & ,DT \le t \le T \end{cases} \tag{3.9}$$

The duty cycle as a function of k is obtained in the same way as in buck mode.

$$D = 1 - k \tag{3.10}$$

The maximum switching frequency is again reached when the LV is half of the HV. The output power on boost mode is calculated using (3.11).

$$P_{out\,boost} = (1-D)V_{HV}i_{L\,avg} \Rightarrow P_{out\,boost} = V_{LV}i_{L\,avg} \tag{3.11}$$

3.2 – The Fast Charger

One of the major drawbacks that people see in EVs (electric vehicles) is the long time that the batteries take to charge. Nowadays fast charging of EV's and its integration on the grid are topics that receive a lot of attention [25][26].

3.2.1 – Intention

In the project under development at ISEL, the idea is to build a universal fast charger that under certain conditions, theoretically, can reach up to 150kW. One of the problems that appears with charging at this power is the impact on a weak electrical grid that happens when 150kW of load appear instantly [26]. To solve this problem a big stationary battery bank will be used and charged directly from the grid at a slow rate. When an EV is plugged in, the energy transferred during the fast charge comes from the stationary battery bank, eliminating the impact on the grid.

In order to have a universal charger, it must support different voltages inputs because the EVs don't have a normalized voltage level of the batteries. For this reason limits of operation need to be defined, those will depend on the hardware used.

The final fast charger design is pretended to be compact, cost effective and energy efficient.

Since this is a prototype, a simplistic approach is taken. In order for ease of control, the continuous direct current and its ripple will be maintained fixed. Analyzing (3.8) and (3.11) it's concluded that, with the direct current been kept constant, the charging power is only dependent of the voltage level of the LV bank. This means that in buck mode, EVs with lower voltage battery banks will charge with at a lower rate than the ones with higher voltage batteries. On the other side if the EV has a higher voltage than the stationary battery bank, the charging power is limited by the voltage of the stationary battery bank.

3.2.2 – Semiconductors

The prototype is expected to be functional. This means that topics such as cost and size optimization aren't mandatory in this stage. The component that imposes most of the limitations to the system is the semiconductor used. In this prototype the chosen semiconductors are SiC (Silicon Carbide) MOSFETs (Metal Oxide Semiconductor Field Effect Transistor) manufactured by CREE. The choice of SiC MOSFET devices was due to its very high efficiency, high switching frequency and high current density when compared to the usual silicon based semiconductors [27]. This choice is expected to result in an more efficient, smaller and lighter converter when compared to a converter using the usual Silicon based semiconductors [28].

3.2.3 – Operation limits

All the components used in the system must support the limits of operation defined by the application designer. These limits are:

- Maximum switching frequency: 100 kHz;
- Maximum continuous current: 300 A;
- Maximum input voltage: 500 V (V_{HV});
- Minimum input voltage: 80 V (V_{LV});
- Peak to peak ripple current: 37.5 A (6.25% of the DC current)

3.2.4 – Inductance required

To obtain the minimum value of inductance required in order to maintain the switching frequency bellow its maximum value, it's necessary to use the equations obtained in the mathematical model and the values of the limits of operation. For both operating modes (buck and boost) the expression of required inductance will be the same. Equation (3.12) calculates the minimum value of inductance. For this calculation the value of k used is the one that leads the converter to the higher switching frequency, this is one half, obtained in (3.7).

$$L_{required} = \frac{k(1-k)V_{HV\max}}{\Delta i_{L\min} f_{\max}} \tag{3.12}$$

Doing the math, the value of inductance reached is 33.33 µH. Such a small value of inductance is obtained due to the high switching frequency of the semiconductors.

3.3 – Numerical simulation model

The simulation was implemented in Matlab Simulink using blocks from SimPowerSystems library. The use of existing blocks instead of the dynamic equations obtained in Section 3.1.3 is because Simulink has dynamic models of various types of batteries and semiconductors which aren't part of the thesis objectives. Figure 3.3 shows the block diagram of the fast charger implemented in Matlab Simulink. The input parameters for the blocks are presented on Table 3.3.

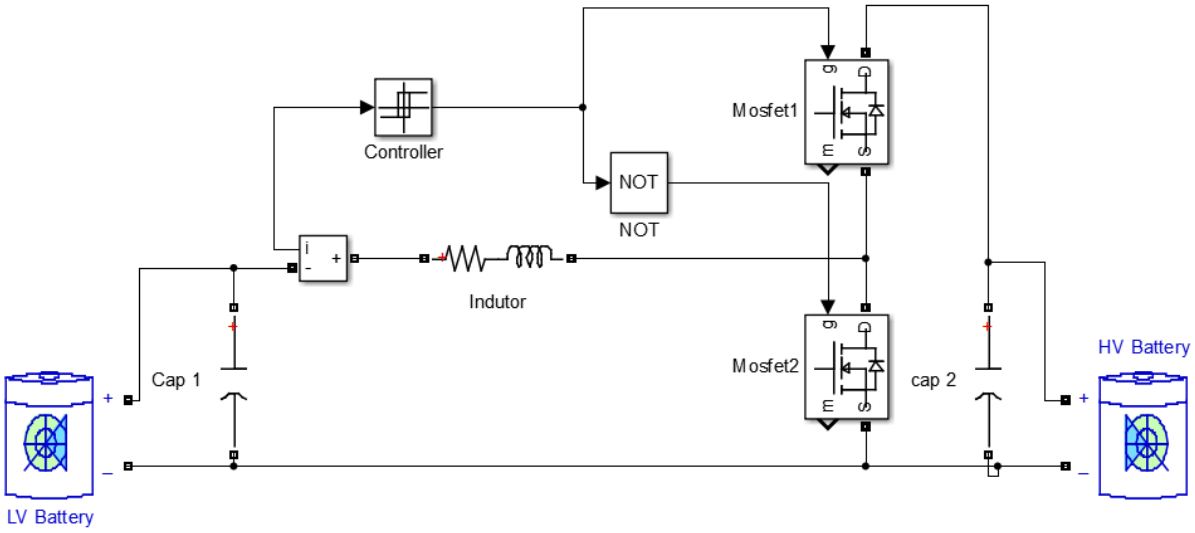

Figure 3.3 – Simulink block diagram of the Fast Charger.

The controller block is a hysteretic controller that receives the value of the inductor current and depending on the operation mode it sends the command signals for the semiconductors. The command signals are orders to open or close the semiconductors, these orders are explained on Table 3.1 and Table 3.2.

Capacitors were inserted in the circuit in order to protect the batteries from big current peaks. This way the capacitors suffer the current peaks and then deliver the energy to the battery

bank with a smoother current wave, increasing the battery bank's lifetime. The comparison between the situation with and the situation without capacitors is done on Figure 3.4. It's possible to observe that in the presence of capacitors, the current in the batteries is smoother while the current in the inductor is the same as in the absence of the capacitors.

Table 3.3 – Numerical Simulation Block inputs

Block	**Parameter**	**Value**
LV Battery	Battery Type	Lithium ion
	Nominal Voltage	220 V
	Initial SOC (state of charge)	50%
HV Battery	Battery Type	Lithium ion
	Nominal Voltage	465 V
	Initial SOC (state of charge)	50%
Inductor Branch	Resistance	0.0007 Ω
	Inductance	33.33 µH
LV and HV Capacitors	Capacitance	220 µF

The objective of the simulation model is to predict the system behavior, helping the designer to understand the conditions that the components are subjected during operation. For this case it is important to verify that the maximum switching frequency of the SiC MOSFETs is respected. In order to verify this, a tool included on Simulink called FFT (Fast Fourier Transform) Analysis was utilized. This tool gives as output the frequency spectrum of a signal during a time interval of simulation. On Figure 3.5 it's presented the spectrum of frequency of the inductor current on both operation modes (buck and boost) for the situation that maximizes the switching frequency. The chosen signal was the inductor current because it represents the sum of the currents of both semiconductors.

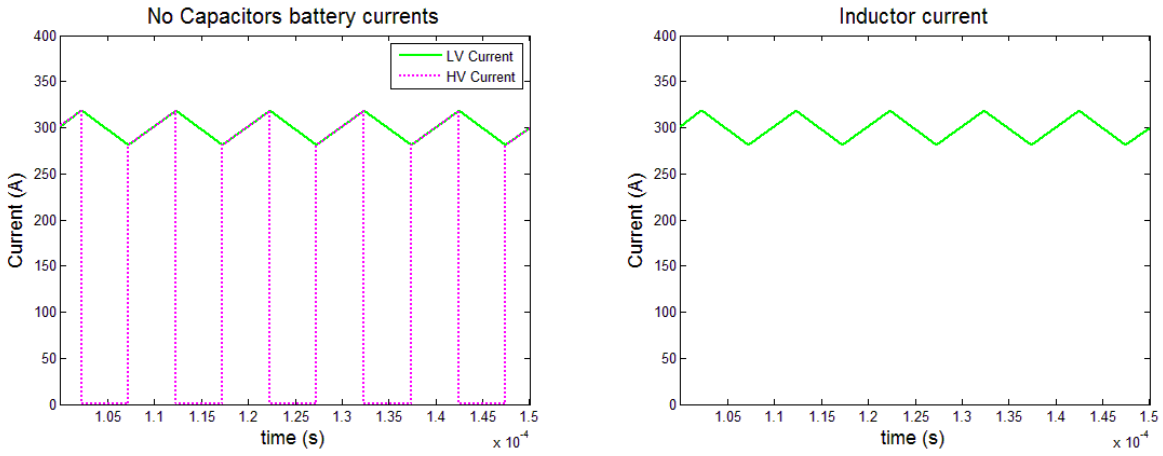

(a)

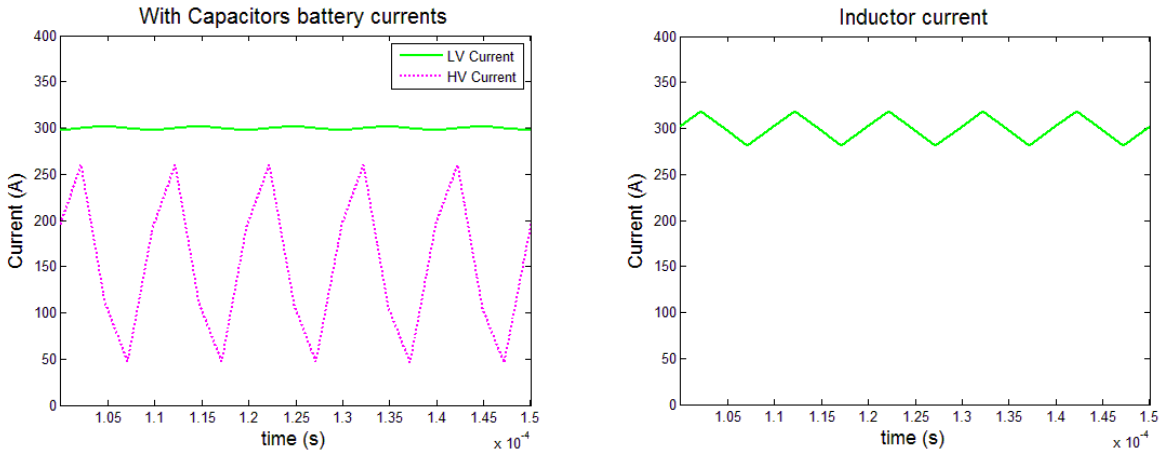

(b)

Figure 3.4 – Comparison between currents in Buck mode for: (a) no capacitors; (b) with capacitors.

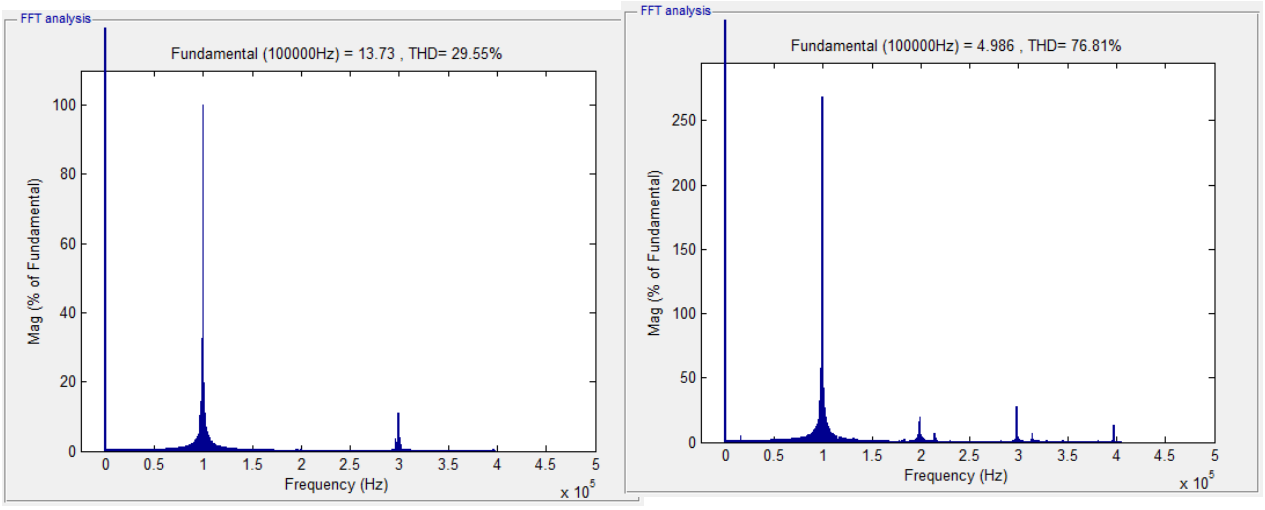

(a) (b)

Figure 3.5 – Frequency spectrum of the inductor current: (a) in Buck mode; (b) in Boost mode.

Analyzing Figure 3.5 it's possible to conclude that in the situation where the frequency is maximized, the current in the inductor has a very high DC component and that the other big component is the 100 kHz. This validates the calculation of required inductance.

3.4 – Inductor Design

The value of inductance required for the fast charger is 33,33 µH. It's now necessary to make decisions on the inductor design based on the application requirements and operating conditions.

For applications that have high DC currents it's important to take into consideration the DC bias effect on the permeability of the core material. The magnetic permeability generally decreases with an applied DC magnetizing force [15]. This is usually controlled by adjusting the air gap length. For distributed air gap cores the curve of the permeability *vs.* DC bias is given by the core's manufacturer on its catalogue. This characteristic indicates how much of the initial permeability of the core is preserved for a dc magnetic field.

3.4.1 – Election of Materials and core shape

As introduced on the previous chapter, there are lots of materials and shapes on the market. When designing an inductor, the engineer can't go through all possible configurations and test them all to choose that one configuration that suits his application better. It's usual to select a set of few materials and then compare the designs. Summing up the materials properties presented in the previous chapter:

- Ferrites are cheap and offer very low core losses at the cost of low saturation flux density and a sharp saturation curve.
- Amorphous and Nanocrystalline materials both offer very high saturation flux density and low core losses at the cost of both being expensive compared with the other materials.
- Powder core materials offer relatively high saturation flux and the distributed air gap which leads to a soft saturation curve. The drawback is its higher core losses compared to the other alternatives.

Based on the defined low percentage value for the current ripple and on very high DC current it's expected that the inductor core losses be small when compared to the winding losses. Expected low core losses, combined with the design priorities of the fast charger, leads to choose the powder core materials as better suited materials for the design. Similar applications are found on the literature comparing powder cores with other materials. Powder core materials show good results in terms of efficiency and inductor size [29][30].

Magnetics Inc. has shown interest and availability to supply the cores for this prototype. On their catalogue they have what it's called core selector charts. In these charts it's possible to know which materials are best suited for the application, based on the existent core sizes. This is done by calculating an image of the value of the energy stored in the inductor.

$$\text{Fast Charger Required } Li^2 \quad (mHA^2) \qquad 3000$$

After consultation of the core selector charts, the materials decided to be part of the study are:

- MPP 14µ;
- MPP 26µ;
- High Flux 14µ;

- High Flux 26µ;
- Kool Mu 26µ

Most of the powder materials are limited to a toroid core shape. From the list of materials included in the study only Kool Mu has the option of toroidal, E shape and U shape cores. In order to narrow the design possibilities, the decision to only consider toroidal core shape for the study was taken. Magnetics Inc. state in their catalogue that the powder material cores have a tolerance of ±8% on its inductance factor. For this reason the on load value of inductance pretended is 36 µH in order to guarantee the required inductance for the converter.

Due to the high value of current that the inductor needs to support, a big area of copper is necessary, for this reason only the toroid cores with the three bigger window areas on the catalogue are considered for the design.

3.4.2 – Inductance calculation method for toroidal powder cores

Figure 3.6 illustrates the dimensions of a toroid core, where *OD* is the outer diameter, *ID* is the inner diameter, *Ht* is the height, A_c is the core's cross section and l_m is the core's magnetic length.

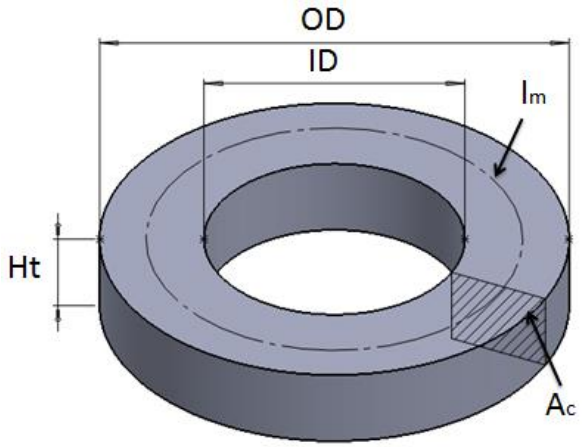

Figure 3.6 – Toroidal core dimensions.

The value of the magnetic circuit length for a toroid with squared cross section is obtained by (3.13).

$$l_m = \frac{\pi(OD - ID)}{\ln\left(\frac{OD}{ID}\right)} \tag{3.13}$$

The inductance factor, introduced on Section 2.2.1 –, is a fast way to know how many turns of wire are needed in order to obtain the pretended inductance, see (3.14).

$$N = \sqrt{\frac{L_{required}}{A_L}} \tag{3.14}$$

The number of turns calculated on (3.14) needs to be corrected due the affected permeability of the core due to the DC magnetizing force [18]. The inductance at a rated current is obtained by (3.15), where μ_{eff} is the effective relative permeability of the material due to the DC field and μ_i is the initial relative permeability of the material.

$$L = N^2 A_L \frac{\mu_{eff}}{\mu_i} \tag{3.15}$$

This is an iterative process in which the effective permeability is calculated and inserted on (3.15), if the inductance value is lower than the required inductance, the number of turns must be incremented and the calculation repeated until the value of required inductance is reached.

The DC bias curves of the materials considered in the design are given on Appendix A.

3.4.3 – Design Strategy

The design includes five materials and three core sizes. Keeping in mind that an inductor can have more than one core and wanting to optimize the inductor for low saturation level and low losses while keeping it compact and cost effective, there are too many configurations to be tested. In order to solve this problem a strategy is proposed, this consists of four stages:

1. Sensibility study (also called Scattering study) using FEA which gives an understanding in how the inductor losses are influenced by the physical dimensions of the core, this was done separately for each of the considered core materials.
2. A grading system is developed which grades the possible configurations for each material taking into account the results of the sensibility study.

3. Test the model of the one or two best configurations of each material using FEA in order to make a final decision on the inductor design.
4. Winding design taking into account losses due to increased AC resistance.

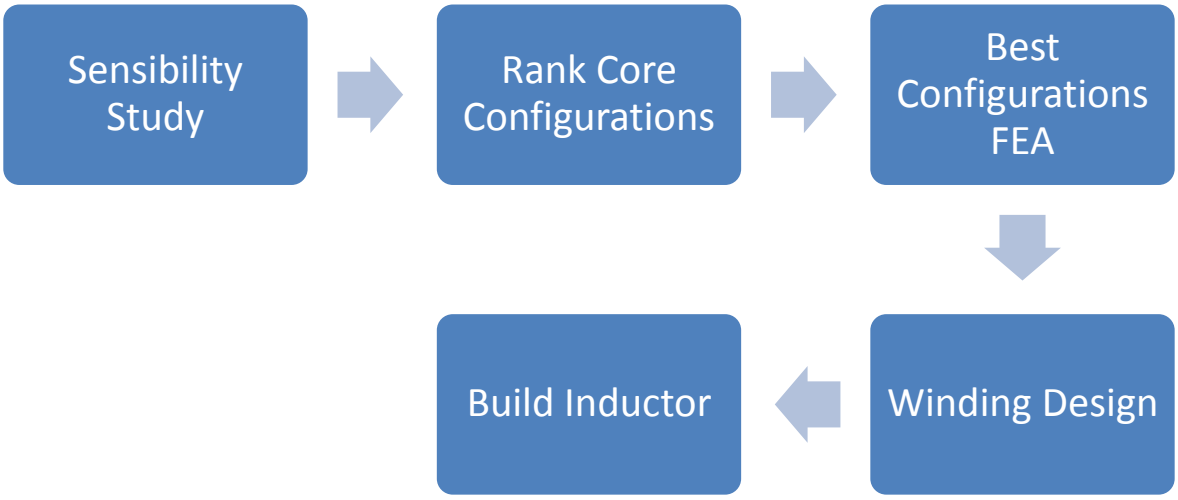

Figure 3.7 – Design strategy flowchart.

3.5 – Conclusions

In this chapter a Fast Charger project is introduced along with its limits of operation. The mathematical model of the BDC topology used in the fast charger is presented and the required value of inductance is calculated. A simulation model is constructed on SIMULINK using SimPowerSystems library blocks that validates the inductance value calculated by the mathematical model developed.

Due to the big number of details and possible choices that exist in the magnetic components design, better and faster design tools and strategies are continuously being updated. An example of this is the electromagnetic FEM software market which is constantly developing new tools to help the design engineer manufacture better products.

The inductor design first's decisions were taken. The materials to be considered in the design are powder core materials from Magnetics Inc. and the core shape will be a toroid. A four stages design strategy which utilizes Finite Element Analysis (FEA) is introduced due to the high number of possible configurations available.

Chapter 4

Inductor Design using Finite Element Method

4.1 – Introduction to Finite Element Method

In the design of electromagnetic components, being these inductors or motors, it's a great advantage and importance the use of tools capable to predict accurately the designed component behavior, while keeping the design cheap and fast. A very good option are the tools based on FEM [31]. These tools give the possibility of testing many configurations, without the need of physically building each of the prototypes, eliminating most of the exhaustive laboratory measurement work. This contributes to a cheaper and more efficient design strategy.

FEM is a numerical method for solving differential equations. Nowadays it's applied in several branches of engineering (e.g. electromagnetism, aeronautics, civil, fluid motion, thermodynamics, nuclear, etc.) [32].

This method is usually applied to study a complex physical model. In the FEM design the model is discretized into a finite number of elements. Those elements share nodes between them, and all together form the Mesh of the problem. Initial and boundaries conditions are defined by the engineer, and then a group of equations is applied to the mesh, solving each element separately in a giant system of equations. The bigger the number of elements is, the more accurate the solution but higher is the processing power required from the computer due to the bigger number of equations to solve, consequently this takes more simulation time.

4.1.1 – Equations Solved

The equations applied to the mesh of the finite element problem depend on the nature of the problem. Electromagnetic problems use a set of four differential equations that unify all

principals of the electromagnetism theory [33], published by James Clerk Maxwell in 1865, those are:

Ampere's law

$$\nabla \times \mathbf{H} = \mathbf{J} + \frac{d\mathbf{D}}{dt} \tag{4.1}$$

Faraday's law

$$\nabla \times \mathbf{E} = -\frac{d\mathbf{B}}{dt} \tag{4.2}$$

Gauss law for electricity

$$\nabla \cdot \mathbf{D} = \rho \tag{4.3}$$

Gauss law for magnetism

$$\nabla \cdot \mathbf{B} = 0 \tag{4.4}$$

Where $\mathbf{H}$ is the magnetic field, $\mathbf{B}$ is the magnetic induction, $\mathbf{E}$ is the electric field, $\mathbf{D}$ is the electric flux density, $\mathbf{J}$ is the current density and ρ is the electric charge volume density.

In addition to Maxwell's equations, it's important to introduce the equations that express the properties of materials, these constitutive relations are:

$$\mathbf{B} = \mu_0 \left(\mathbf{H} + \mathbf{M} \right) \tag{4.5}$$

$$\mathbf{D} = \varepsilon \mathbf{E} \tag{4.6}$$

$$\mathbf{J} = \sigma \mathbf{E} \tag{4.7}$$

Where $\mathbf{M}$ is the magnetization vector.

4.1.2 – FEM Models

As stated on Chapter 1 the FEA software used in this thesis was Ansys Maxwell. Two different solvers have been utilized. Magnetostatic solver was used to calculate inductance under different DC bias conditions. The inductor losses have been calculated using Transient Magnetic solver.

Each solver is used for a specific type of electromagnetic problem, this means that even though all equations from (4.1) to (4.7) need to be verified, each solver utilize specific assumptions that make the results depend on a minor set of equations in order to lighten the processing work. For non-time dependent solvers the software provides the function of adaptive meshing. This tool creates an initial mesh and refines the mesh at each adaptive pass until convergence of the solution is reached. More information about each specific solver and equations solved is available on the software manuals.

In this thesis four FEA models were created: two 2D, shown in Table 4.1, and two 3D models shown in Table 4.2. The 2D models were created to reduce the computation time in relation with the 3D models. This approach is common in FEA literature [31][34] and is applied on a toroidal inductor in [35][36] with good results in terms of accuracy and a giant computing time reduction in the 2D vs 3D simulation. The stranded winding models were created to conduct the pre-winding design FEA, this means that the winding is approximated by a solid block of copper wrapped around the toroidal core with an excitation current that is the actual current multiplied by the number of turns of the inductor under simulation. This is because the winding design is the last stage of the design strategy. The results obtained from each of the models are compared later in this chapter.

Table 4.1 – 2D FEA Models

2D Stranded Winding Model	
Model	Mesh
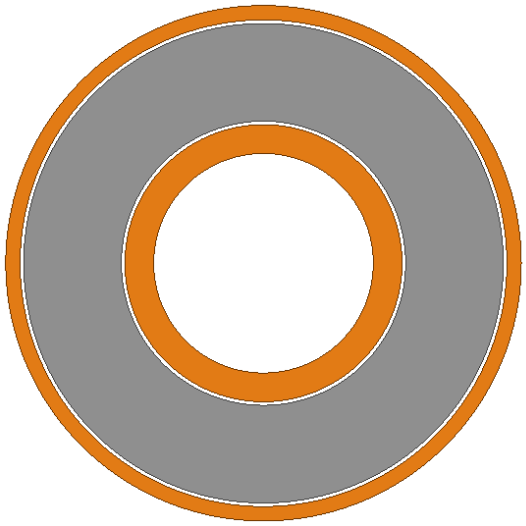	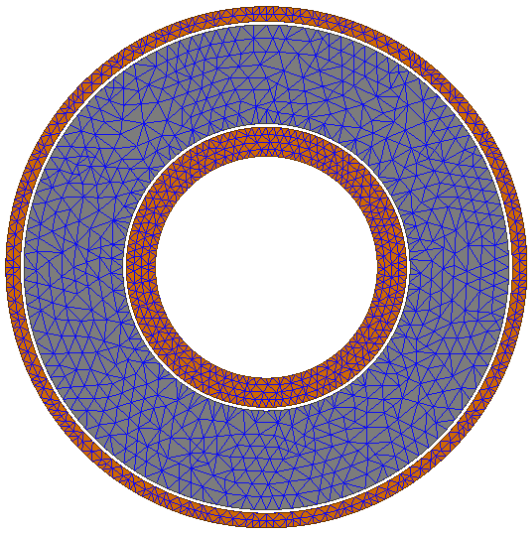
2D Real Winding Model	
Model	Mesh
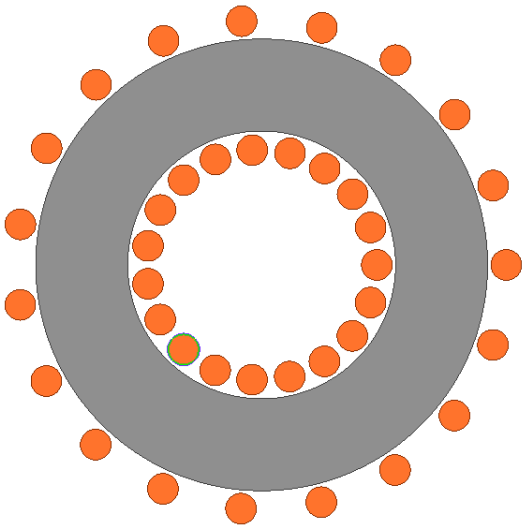	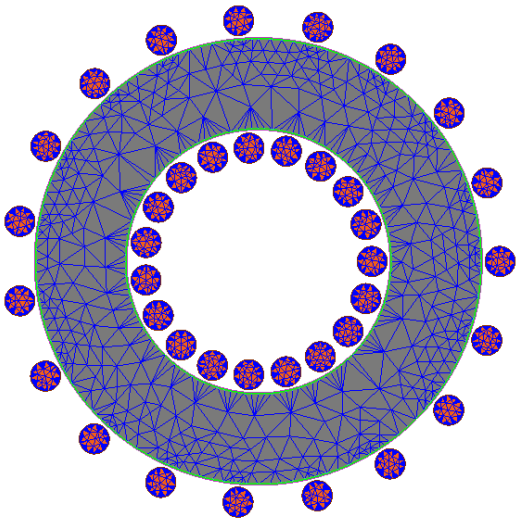

Table 4.2 – 3D FEA Models.

3D Stranded Winding Model	
Model	Mesh
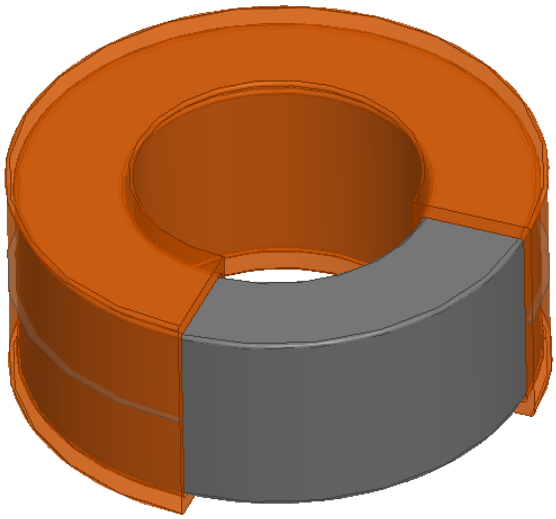	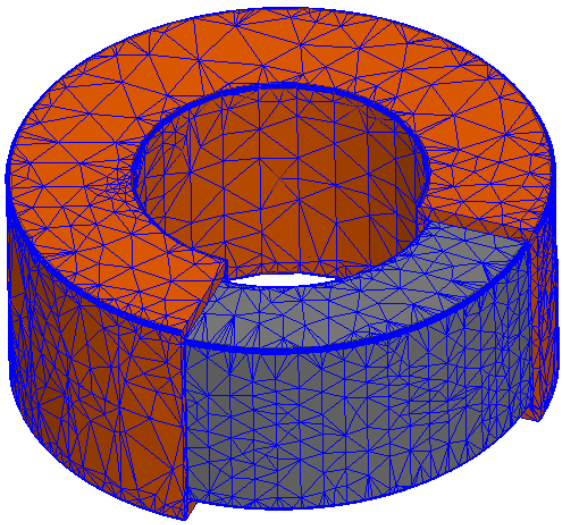
3D Real Winding Model	
Model	Mesh
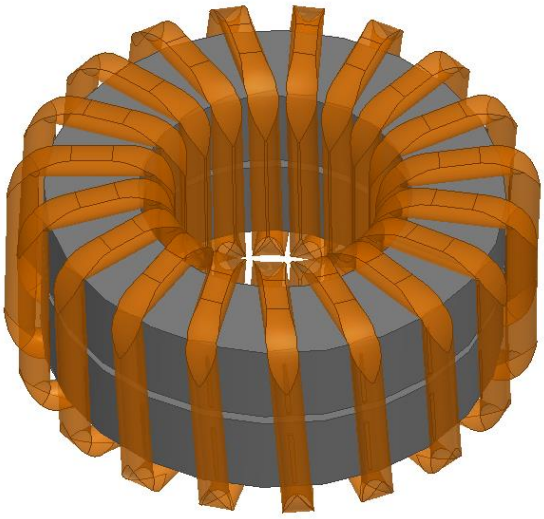	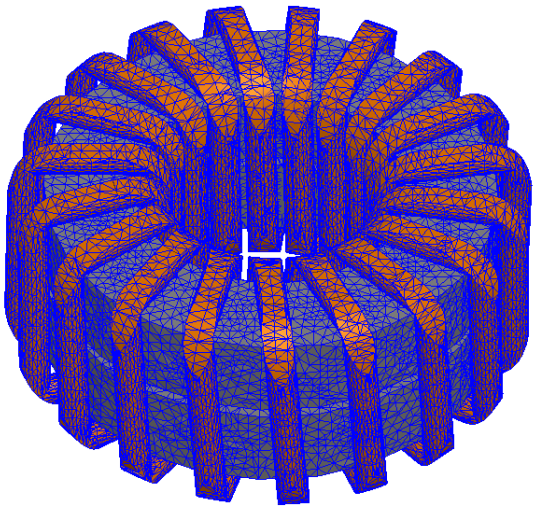

4.2 – Sensibility Study

The objective of a sensibility study is to understand how much a design parameter contributes to the design outputs. In industrial engineering with very complex processes it's common to

perform sensibility studies to determine the key factors in a specific process. This will tell to engineers which process part they should interfere in order to obtain a better output from the process [37].

In this thesis it's pretended to quantify the effect of the geometric parameters of the toroidal core (magnetic length and cross section) on the losses of the inductor. In order to achieve this, it's used a technique called Design of Experiments (DoE). On Figure 4.1 it's presented a schematic that shows how the sensibility study is performed.

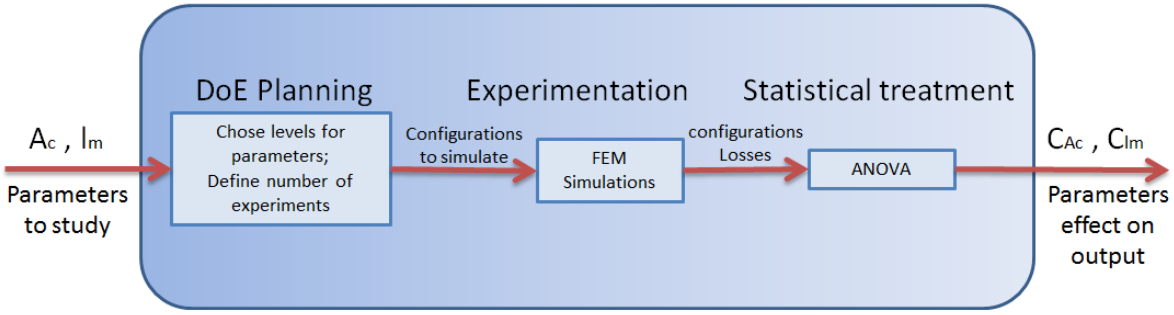

Figure 4.1 – Sensibility study schematic.

4.2.1 – Introducing Design of Experiments

DoE is the science of experimentation. It's a technique that creates a plan of experiments to be performed and then applies statistical tools in order to extract the most information possible from the experiments done [37]. Allying DoE to FEA is common on engineering designs and creates a great optimization tool. Examples of designs that combine both technics are found in [34][38][39].

There are two possible approaches on DoE. These are: Full Factorial Design and Fractional Factorial Design. The difference of these techniques is the number of experiments done. In the full factorial design all the possible combinations of levels between factors must be tested, while on the second only a fraction of the experiments takes place. Both have advantages and disadvantages. The full factorial design gives more complete and accurate results because it takes into account the interactions between the factors. On the fractional factorial design these interaction effects are overlapped with the main effects and by other interaction effects[40].

The reason to choose fractional factorial design is the lower cost and lower duration of experimentation which in some occasions is of big concern. In this thesis the duration and

cost of the experimentation phase isn't of big preoccupation since the results will be obtained from FEA. For these reasons the full factorial design is the chosen technique.

4.2.2 – Planning the DoE

The decision to separate the study per material during the statistical analysis stage was taken. This will result in five different statistical studies, one per each material. It's been decided in this way because each material has its own saturation flux, loss curve and magnetic permeability. Considering one material at a time will give better understanding on how the geometry dimensions affect the inductor losses for a specific material, while avoiding that the saturation of one core configuration affects the overall expected performance of the other materials.

The geometry dimensions in the toroidal core geometry that are believed to have bigger impact on the performance of the inductor are its magnetic length (l_m) and the core's cross section (A_c). These are the control factors, also called parameters, of the DoE.

Levels are attributed to each parameter that represents the different conditions of each factor. In this case the levels are associated with the physical dimensions of the parameter. All the possible configurations made from the different levels of the parameters constitute the sample of the statistical study.

In this study both the parameters will be divided in three levels. The magnetic length will be exactly the ones that appear on the three biggest toroid cores on the Magnetics Inc. catalogue, while the core's cross section will be studied in values that are considered suitable for the application. On Table 4.3 are presented the DoE parameters and its levels for this study.

Table 4.3 – DoE parameters and its levels.

	Levels		
Parameters	0	1	2
Core's Cross Section [cm^2]	15	30	50
Magnetic Length [cm]	24.3	32.4	41.2

It's important that the same conditions are verified on all experiments. This means that every configuration must have the same or a close value of inductance. Varying geometric dimensions affect the value of inductance of the magnetic component being simulated, for this reason and also because of the saturation under DC bias conditions the wire number of turns is corrected for every configuration.

Because the statistical treatment is equal for all the materials, only the treatment of the material High Flux 26µ will be presented in this section. Table 4.4 presents the configurations tested for the High Flux 26µ. The table with all configurations tested, inputs for the FEA model and its results for all the materials are presented on Appendix B.

Table 4.4 – Table of experiments for the High Flux 26µ.

Configuration	A_c level	l_m level	Wire turns
1	0	0	16
2	0	1	18
3	0	2	19
4	1	0	11
5	1	1	12
6	1	2	13
7	2	0	8
8	2	1	9
9	2	2	10

The outputs from FEA will be the inductance on no-load and on load conditions and the core losses under the fast charger operating conditions ($D = 0.5$; $f = 100$ kHz ; $I_{dc} = 300\,\text{A}$; $\Delta I = 37.5\,\text{A}$). In order to obtain the inductor losses, the windings losses are necessary. As seen on Chapter 2 the winding losses are divided into AC and DC losses. Since AC losses are mainly dependent on the winding arrangements, these aren't taken into account for the

sensibility study. The DC winding losses are calculated assuming the copper conductivity at 20 degree Celsius. The DC resistance of the winding is calculated by (4.8) , where MLT is the mean length per turn of wire for the configuration under test. The wire area has been chosen in order to have a current density of 300 A/cm^2 on the wire section.

$$R_{dc} = \frac{NMLT}{\sigma A_{wire}} \tag{4.8}$$

The DC winding losses are added to the core losses and those are considered together as the inductor losses.

4.2.3 – DoE results

The results of each configuration of High Flux 26µ are presented on Table 4.5. The losses are shown in form of graph on Figure 4.2. Graph form is ideal to look for interactions between the parameters. Analyzing the graph it's possible to conclude that no significant interactions are present on this material under the tested conditions. This is concluded because the inductor losses lines on the graph are approximately parallel between the different levels of core's cross section and magnetic length. This isn't true for all materials and some interactions are seen on configurations in which the material starts to saturate. The full table of the DoE results is given on Appendix B.

Analysis of Variance (ANOVA) is a statistical tool that in this case is applied to quantify how much each of the parameters affects the losses. The ANOVA table has been calculated using the function "anovan" existent in MATLAB. The results of ANOVA are shown on Figure 4.3.

Table 4.5 – Results for the High Flux 26µ.

Configuration	$L_{no-load}\ [\mu H]$	$L_{load}\ [\mu H]$	Core Losses [W]	DC Copper Losses [W]	Inductor Losses [W]
1	54.02	37.91	7.69	55.0	62.7
2	51.45	39.32	13.01	55.5	68.6
3	45.12	37.17	19.64	56.0	75.7
4	50.79	42.27	23.04	62.4	85.5
5	45.41	39.86	30.03	57.1	87.1
6	41.98	38.06	33.89	55.5	89.4
7	44.59	40.20	33.84	69.2	103.1
8	42.42	39.30	38.08	62.9	101.0
9	41.58	39.13	40.27	60.3	100.5

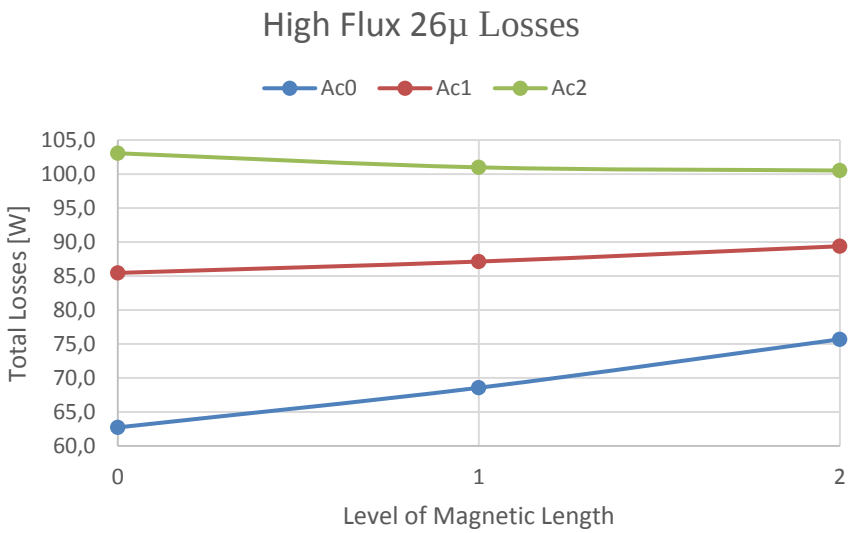

Figure 4.2 – DoE losses results for the High Flux 26µ.

Analysis of Variance

Source	Sum Sq.	d.f.	Mean Sq.	F	Prob>F
Cross Section	1596.58	2	798.289	52.55	0.0013
Magnetic Length	34.95	2	17.474	1.15	0.403
Error	60.76	4	15.191		
Total	1692.29	8			

Figure 4.3 – ANOVA table for the Losses of High Flux 26µ.

The percentage contribution of each parameter is calculated dividing its sum of squares by the total sum of squares. The percentage contribution of each parameter to the inductor losses is presented on Table 4.6.

Table 4.6 – Percentage contribution of the DoE parameters for High Flux 26µ.

Parameter	Percentage Contribution
Core's Cross Section	94%
Magnetic Length	2%
Error	4%

It's concluded that for High Flux 26µ the only parameter that has significant influence on the inductor losses is the core's cross section. The lower the cross section the lower the losses, this is explained by a big increase in core losses when the core's cross section is augmented and a small increase in copper losses.

4.3 – Configurations Evaluation

At this point it's known how much each parameter affects the inductor losses. Now it's important to classify all the possible core configurations in order to create a ranking of configurations per material. The best inductors are simulated on Ansys Maxwell in order to choose the best inductor.

4.3.1 – Grading System

The overall idea is to give a score for each specific core configuration with a core's cross section between 9 and 50 cm^2, and with the magnetic lengths used in the sensibility study. This score takes into account the predicted inductor losses and its percentage of the initial inductance on load conditions. This functions as a measure of saturation that gives the saturation score. The percentage of the initial inductance is calculated as introduced in Section 3.4.2, while the inductor loss score is calculated by (4.9), where S is the loss score of the parameters and C is the percentage contribution of each parameter obtained on the sensibility study.

$$S_{Loss} = S_{l_m} C_{l_m} + S_{A_c} C_{A_c} \tag{4.9}$$

The loss score of the parameters is calculated by linearizing the mean inductor losses of the different levels from the sensibility study. For High Flux 26µ the mean losses per level are presented on Table 4.7.

Table 4.7 – High Flux 26µ DoE mean results

Parameter	Level	Absolute value	Mean Losses [W]
Core's Cross Section A_c	0	15 [cm^2]	69.0
	1	30 [cm^2]	87.3
	2	50 [cm^2]	101.5
Magnetic Length l_m	0	24.3 [cm]	83.7
	1	32.4 [cm]	85.6
	2	41.2 [cm]	88.5

The best performance receives one hundred points, while the worst receives zero points. The intermediate values receive a portion of the points that depends linearly from its position on the interval between the maximum and minimum value of losses. This means that they score more if they are closer to the best, and less if closer to the worst performance.

The total score of the configuration is given by the weighted mean of the score due to losses and to saturation, this is given by (4.10). The study was done with four weights. The weight given to inductor losses was in all situations bigger than 65%.

$$S_{total} = w_{Loss} S_{Loss} + w_{sat} S_{sat} \tag{4.10}$$

The maximum wire fill factor was decided to be 50%. A configuration can have good scores in terms of saturation and losses but if it doesn't have a window area sufficiently large to fill the necessary copper, its score will be null, disqualifying the configuration. The rankings including all the configurations for the different materials are given on Appendix C.

4.3.2 – Better graded configurations

Each material had one sensibility study and the classifications were based on its own study. For this reason at least one configuration per material must be simulated on Ansys Maxwell. The most promising configurations of the ranking are shown in Table 4.8, the results of simulation are presented in Table 4.9 and the dimension characteristics in Table 4.10.

Table 4.8 – Best graded core configurations

Core Config.	Material	Core Ref.	Number of Cores	Cross Section	Magnetic Length	Saturation Score	Losses Score
1	MPP 14µ	OD165.1	1	9.87	41.2	69	89
2	MPP 14µ	OD132.6	3	20.34	32.4	85	80
3	MPP 26µ	OD165.1	3	29.61	41.2	83	81
4	High Flux 14µ	OD165.1	1	9.87	41.2	88	83
5	High Flux 26µ	OD165.1	1	9.87	41.2	74	92
6	High Flux 26µ	OD132.6	2	13.56	32.4	76	82
7	Kool Mu 26µ	OD165.1	3	29.61	41.2	72	89

Table 4.9 – Results for the best graded configurations

Core Config.	Wire Turns	$L_{no\ load}$ [µH]	L_{Load} [µH]	$L_{load}/L_{no\ load}$	Core Loss [W]	DC Copper Loss [W]	Total Losses [W]
1	35	58.8	37.4	0.64	0.4	96.4	96.9
2	20	48.0	38.5	0.80	3.3	81.8	85.4
3	14	49.1	40.1	0.82	3.3	67.5	70.7
4	31	46.7	39.8	0.85	13.7	85.4	99.1
5	25	54.1	38.4	0.71	9.5	68.9	78.3
6	19	53.7	39.3	0.73	11.9	61.9	73.7
7	15	56.9	40.0	0.70	5.2	72.3	77.5

Table 4.10 – Best graded configurations dimensions. Volume unit is cm^3, weight unit is Kg.

Core Config.	Material	Core		Copper		Total	
		Volume	Weight	Volume	Weight	Volume	Weight
1	MPP 14µ	407	2.8	619	5.5	1026	8.3
2	MPP 14µ	659	4.75	526	4.7	1185	9.4
3	MPP 26µ	1220	9	433	3.9	1653	12.9
4	High Flux 14µ	407	2.6	549	4.9	955	7.5
5	High Flux 26µ	407	2.8	442	4	849	6.8
6	High Flux 26µ	439	3	397	3.6	837	6.6
7	Kool Mu 26µ	1220	6.6	434	4.2	1684	10.8

Analyzing Table 4.9 and Table 4.10 it's concluded that the best configuration is the sixth. This configuration has 2 cores of High Flux 26µ with an outer diameter of 132.6mm and 19 turns of wire. This is chosen as the best configuration because it's placed as second on losses

performance and its percentage of initial inductance is above 70% while having the lower volume and weight of all the best graded configurations.

4.4 – Winding design

Due to the toroidal inductor geometry, foil windings are considered not feasible for this situation. For this reason only solid and litz wire are considered in this design. The situation under study is the fast charger inductor current with a switching frequency of 100 kHz and a duty cycle of 0.5.

4.4.1 – Solid Wire

Solid wire has the advantage of lower cost than with litz wire. Its disadvantage is its high losses under high frequency AC currents.

For this study different wire diameter sizes are studied with different current densities. The variation of current density is done adjusting the number of parallel branches of wire. The method used to calculate the AC winding losses is he one introduced on Section 2.2.4, presented in [11]. This approach needs an approximation for the toroidal geometry, since there will be more inner layers than outer layers due to different inner and outer diameter of the toroid. Current harmonics up to order 35 were considered. After this analytical approach, a FEA took place in order to validate the results and obtain the best configuration.

Wire diameter sizes from 3.5mm to 5mm are considered and current densities from 3 A/mm^2 to 5 A/mm^2. The range of wire diameters was chosen taking into account that a one layer winding toroid isn't possible due to the high current involved in the fast charger. On the other hand, the consideration of higher wire diameter sizes becomes unpractical making the coil realization difficult on the toroidal core. The 19 turns of wire needed for the toroidal winding in a single layer would be the optimal configuration in terms of copper losses and in parasitic capacitances [41]. According to (2.13) the AC winding losses increase very rapidly when an additional layer of winding is added, winding configurations with a diameter lower than 3.5mm had four layers of winding, decreasing the losses due to skin effect but increasing at a higher rate the losses due to proximity effect. Also important was the fact that the wire was

coiled by hand, this means that very large diameters were difficult to bend while very small diameters would require a big number of parallel branches.

The results of copper losses for the considered winding arrangements are shown on Figure 4.4. It's possible to observe a Pareto front on the graph. The full table of results that gave origin to Figure 4.4 is presented on Appendix D. The winding configurations that form the Pareto front are given on Table 4.11.

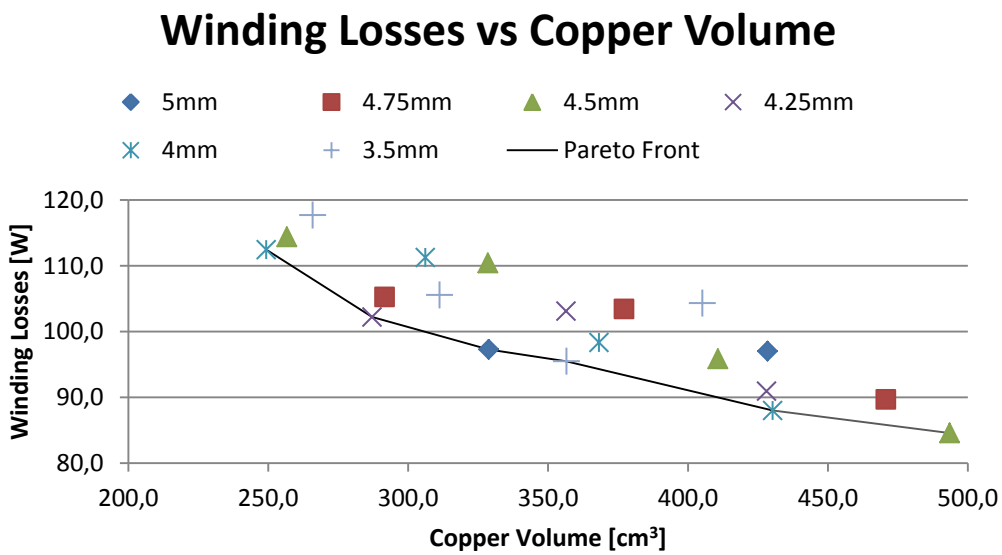

Figure 4.4 – Results of different winding arrangements of winding losses vs copper volume.

After analyzing Figure 4.4 and Table 4.11 the chosen configurations to be studied with FEA are: the configuration with 9 parallel branches of 3.5mm diameter wire and the configuration with 4 parallel branches of 5mm diameter wire. This choice is due to being configurations with moderate winding losses without requiring big quantities of copper. Also after FEA, it gives information on what is more important for this inductor, if the skin effect or the proximity effect.

Table 4.11 – Best Solid wire configurations.

Diameter [mm]	A_{wire} [mm^2]	Parallel branches	Wire layers	J [A/mm^2]	R_{dc} [mΩ]	P_{dc} [W]	P_{ac} [W]	P_{wire} [W]	Cu Volume [cm^3]
5	19.6	4	2	3.8	0.95	85.4	11.9	97.3	329
4.5	15.9	7	3	2.7	0.71	63.8	20.8	84.6	494
4.25	14.2	7	3	3	0.77	69.5	21.4	90.9	428
4	12.6	8	3	3	0.76	68.2	19.8	88	430
4	12.6	5	2	4.8	1.12	101.2	11.3	112.5	249
3.5	9.6	9	3	3.5	0.85	76.2	19.3	107.4	357

The winding FEA has been conducted on the 2D real winding model. The results of winding current density, core flux density and model losses for the 3.5mm and 5mm diameter configurations are presented on Table 4.12 and Table 4.13 respectively.

The copper losses calculated by the 2D model only consider the winding losses from the inner and outer side of the toroid. The top and bottom wires are not included in the FEA results. This means that the results must be adapted to 3D. In order to do this equation (4.11) is applied, where the winding losses obtained from the 2D real winding FEA model are multiplied by a factor which represents how many times the 3D copper losses under DC excitation (given on Table 4.11) are bigger than the 2D copper losses which are an output from the FEA. The final results are shown on Table 4.14.

$$P_{cu\,3D} = P_{cu\,2D}\,\frac{P_{cu\,dc\,3D}}{P_{cu\,dc\,2D}} \tag{4.11}$$

Table 4.12 – 3.5mm solid wire FEA results.

9 Parallel branches of 3.5mm solid wire		
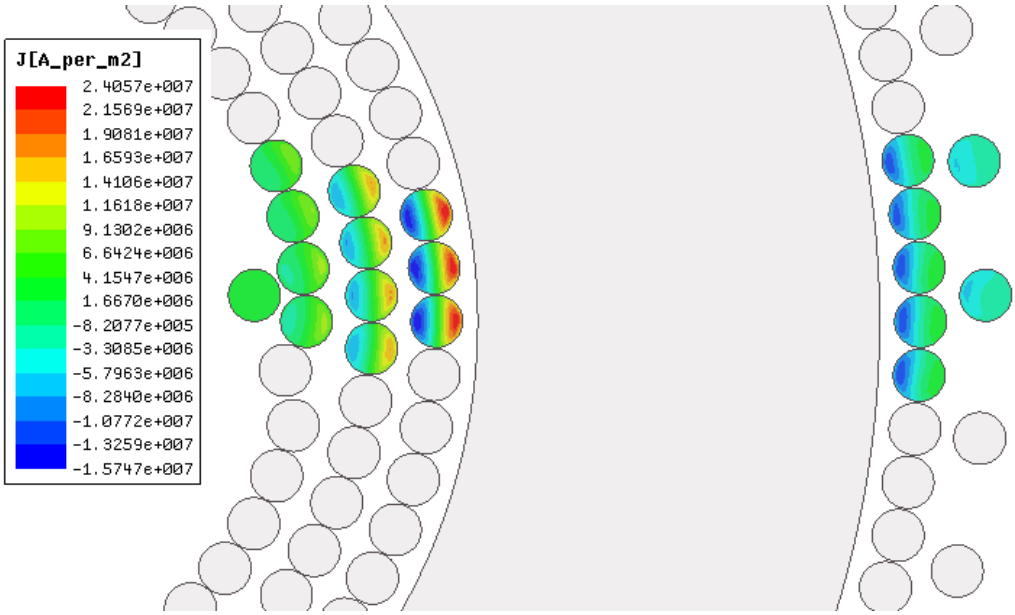		
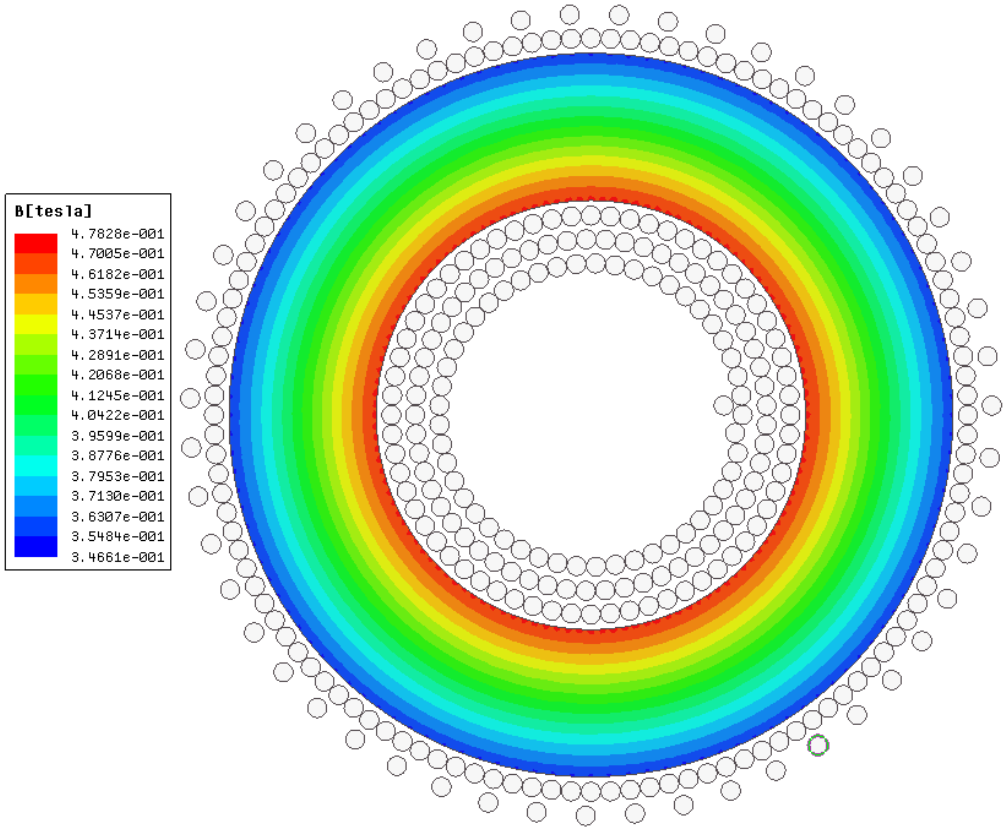		
$P_{core} = 15.1[W]$	$P_{cu\,dc} = 35.7[W]$	$P_{cu\,(ac+dc)} = 48.4[W]$

Table 4.13 – 5mm solid wire FEA results.

<table>
<tr><td colspan="3">4 Parallel branches of 5mm solid wire</td></tr>
<tr><td colspan="3"> 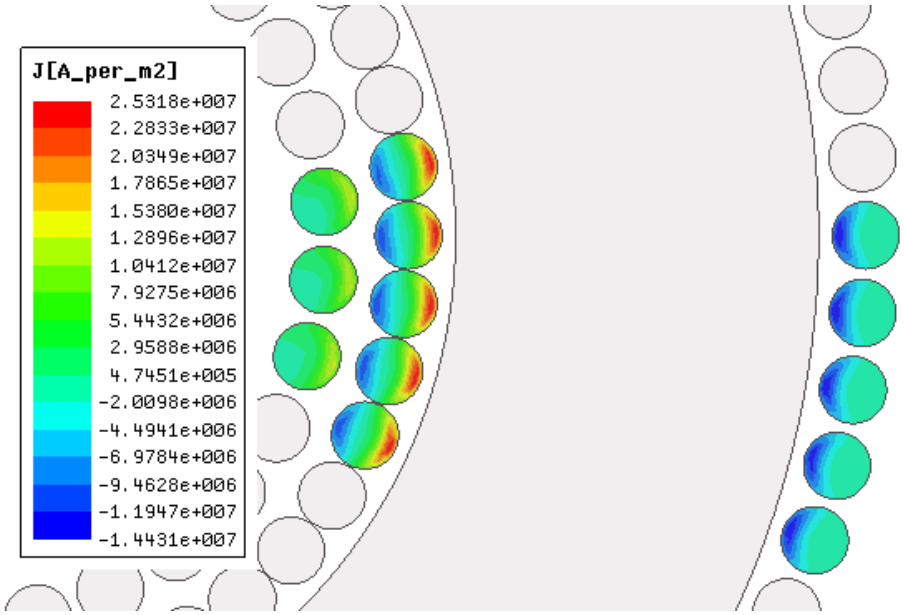
</td></tr>
<tr><td colspan="3"> 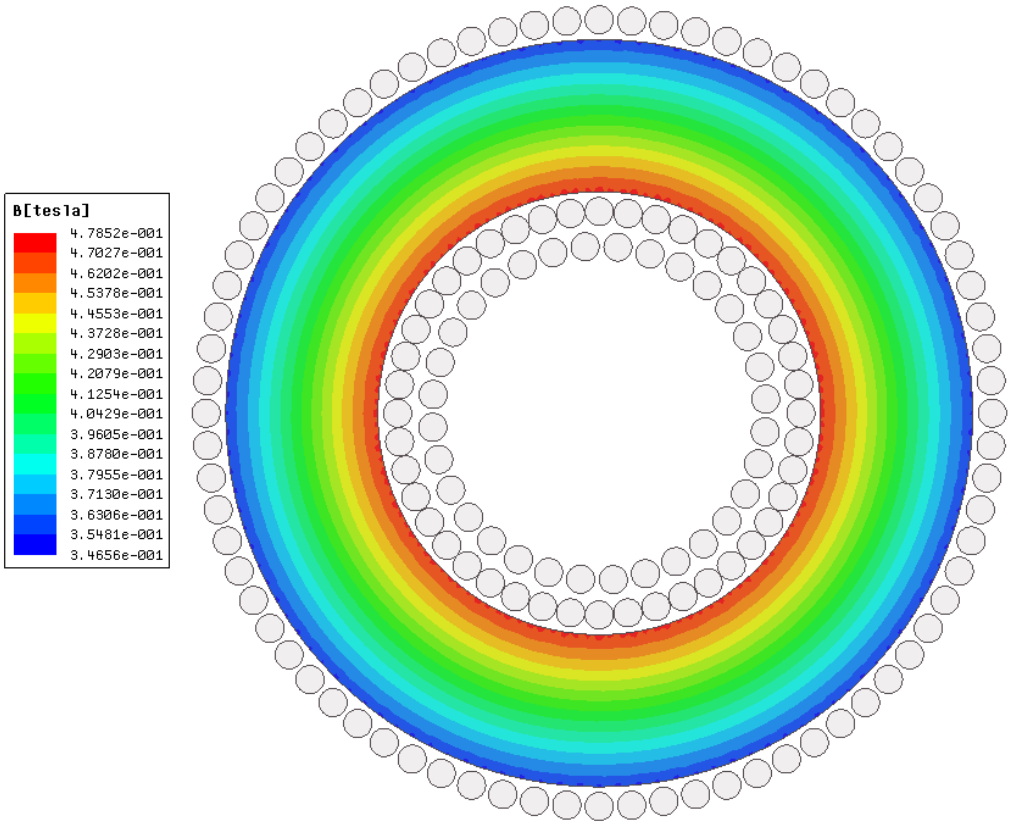
</td></tr>
<tr><td>$P_{core} = 21[W]$</td><td>$P_{cu\,dc} = 39.4[W]$</td><td>$P_{cu\,(ac+dc)} = 68.2[W]$</td></tr>
</table>

Table 4.14 – Final solid winding design results.

Configuration diameter [mm]	Core Losses [W]	Winding Losses [W]	Inductor Losses [W]	Copper Volume [cm^3]
3.5	15.1	103.3	118.4	357
5	21	148	169	329

The FEA results show discordance with the analytical results, principally for the second configuration. This may be because the approximation taken on the analytical calculations which ignored that a toroidal core has a bigger number of layers on the inside than on the outside of the toroid. Other conclusion that can be done is that the winding arrangement has impact on the core losses of the inductor. This is explained by stronger magnetic flux density on the regions near the winding, this is seen on the images from Table 4.12 and Table 4.13.

The final decision is to consider as the best solid winding arrangement the configuration with 9 parallel branches of 3.5mm diameter wire.

4.4.2 – Litz wire

For this type of winding, a simplified design method for litz wire has been adopted, this is introduced in [42]. This design method is divided into steps.

First, in the case of non-sinusoidal current waveforms, the skin depth for the effective frequency (f_{eff}) is calculated. Effective frequency is introduced and explained in more detail by [42]. Effective frequency is calculated by (4.12).

$$f_{eff} = \frac{\left(\frac{di_L(t)}{dt}\right)_{rms}}{2\pi I_{ac\,rms}} \tag{4.12}$$

The recommended number of strands is calculated by (4.13), where b is the breadth of the core, h is a constant for each strand diameter and n_e is the recommended number of strands. It's advised in the method to consider a maximum window fill factor of 30% due to the high quantity of isolation and twist operations inherent to the litz cables.

$$n_e = \frac{h\delta^2 b}{N} \tag{4.13}$$

Then the ratio of AC to DC resistance is calculated by (4.14), where n is the number of strands actually used and d_s is the strand diameter.

$$\frac{R_{ac}}{R_{dc}} = 1 + \frac{(\pi n N)^2 d_s^{\,6}}{192\delta^4 b^2} \tag{4.14}$$

Everything that is needed to calculate the litz winding losses is known. This is calculated by (2.17) introduced on chapter 2. The results obtained are shown on Table 4.15.

Table 4.15 – Litz wire design results.

AWG strand size	Strand diameter [mm]	h [mm^{-3}]	n_e	n	% window area	R_{dc} [mΩ]	$\frac{R_{ac}}{R_{dc}}$	J [A/mm^2]	P_{dc} [W]	P_{ac} [W]	P_{wire} [W]
32	0.202	130	671	700	8.4	3.06	1.002	13.9	276	0.4	276
33	0.18	203	1048	1000	10.4	2.70	1.003	11.2	243	0.3	243
34	0.16	318	1642	1650	12.9	2.07	1.003	9.1	186	0.20	187
35	0.143	496	2561	2600	16.1	1.65	1.004	7.3	148	0.2	148
36	0.127	771	3981	4000	19.7	1.36	1.005	5.9	122	0.2	122
37	0.113	1200	6196	6300	24.3	1.09	1.006	4.8	98	0.1	98
38	0.101	1800	9294	9200	29.2	0.93	1.007	4.0	84	0.1	84
39	0.09	2800	14457	14500	36	0.75	1.009	3.3	67	0.1	67
40	0.08	4400	22719	22500	44.7	0.61	1.010	2.6	55	0.1	55
41	0.071	6700	34594	34400	53.6	0.50	1.012	2.2	45	0.1	46
42	0.063	10000	51633	52000	63	0.42	1.013	1.9	38	0.1	38

It’s seen that the AWG strand size that leads to the lowest winding losses while respecting the 30% of maximum window filled area is the AWG 38 strand. This leads to a configuration that has 84W of winding losses.

4.4.3 – Winding Choice

Comparing the best solid wire configuration with 9 parallel branches of 3.5mm diameter wire that leads to 103W of losses in copper, against the best litz wire configuration with 9200 strands of AWG 38 leading to 84W of winding losses, it's decided to go for the solid wire. This design choice considers that the much higher price paid for the litz wire is not worth the 19W of lower copper losses. These results are coherent with the analysis done in [43] where it's been concluded that litz wire don't offer great advantage over solid wire for very small ripple currents which is the case of this converter. Also on [43] are given the different topologies of winding common prices that were taken into account on the final decision for solid wire.

4.5 – Operating Temperature

The inductor losses generate heat which increases the inductor temperature. The rise in the temperature of the inductor must be kept within safe values that depend on the maximum temperature supported by the wire's isolation and by the core's material. It's stated on the Magnetics Inc. catalogue that all the powder cores can operate up to a maximum continuous temperature of 200°C. The typical wire isolation can support up to 150°C. With this said it's important to confirm that the inductor won't overheat during operation. In order to determine the temperature rise of the inductor, an empirical formula encountered in almost every core manufacturer catalogue (including Magnetics Inc.) is used, this is given by (4.15). Where $P_{inductor}$ is the total inductor loss in miliWatt, A_{surf} is the component surface area exposed to the air in squared centimeters and T_{rise} is the temperature rise in degree Celsius.

$$T_{rise} = \left(\frac{P_{inductor}}{A_{surf}} \right)^{0.833} \tag{4.15}$$

The temperature rise represents the increase in temperature in respect to the ambient temperature that the component needs in order to dissipate its losses. This means that the operating temperature, T_{op}, of the component will be the rise in its temperature added to the ambient temperature.

$$T_{op} = T_{rise} + T_{amb} \tag{4.16}$$

It's known that the copper resistivity increases with the increase of its temperature, this will result in higher copper losses and can be calculated by (4.17), where α is copper's temperature coefficient of resistance and $20°C$ is the reference temperature.

$$R_{cu\,T_{op}} = R_{cu\,20°C}\left[1+\alpha\left(T_{op}-20\right)\right] \tag{4.17}$$

In order to calculate the temperature rise of the inductor, a system with the last three equations must be solved. Table 4.16 sums the temperature calculations for the designed inductor considering an ambient temperature of 30°C and a copper temperature coefficient of resistance of $0.004041K^{-1}$.

Table 4.16 – Temperature calculations for the designed inductor.

A_{surf} [cm^3]	$P_{winding}$ [W]	$P_{inductor}$ [W]	T_{rise} [°C]	T_{op} [°C]
728.1	144.7	159.8	89	119

4.6 – Final Inductor and FEA Models comparison

The inductor used in the fast charger has two cores, with outer diameter 132.6mm, of High Flux 26μ, with reference 58337 on Magnetics Inc. catalogue. The winding has 19 turns and is composed by 9 parallel branches of 3.5mm diameter solid copper wire.

The inductance vs DC current characteristic of the inductor obtained from the different FEA models and analytically is shown on Figure 4.5. It's important to say that the 3D real winding model was simulated with a 9mm solid wire instead of the final winding. This was because the 3D geometry was highly complex to draw and highly heavy to simulate if more than 1 layer of winding was used and 9mm corresponded wire diameter that entirely fills the first winding layer. Also observing the results it's possible to observe that all the methods show very similar results, which indicates that adding the extra layers of wire to the 3D model wouldn't make the model much more accurate. The "Analytical method" curve corresponds to the inductance deduction made on chapter 2.

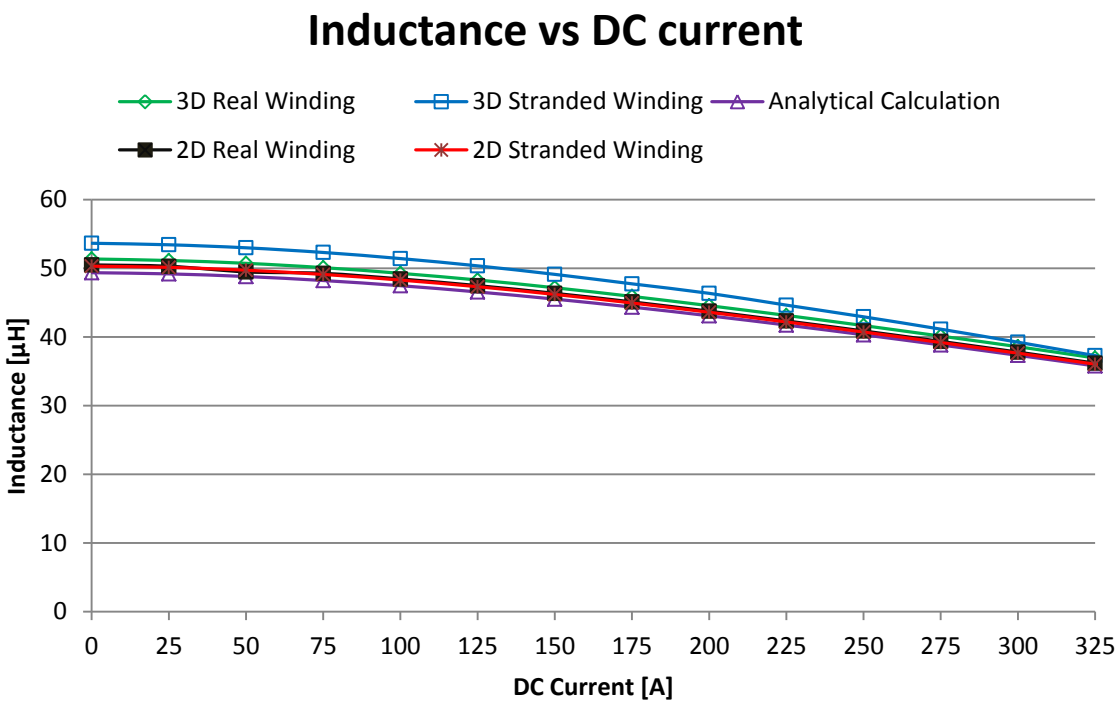

Figure 4.5 – Inductance in function of DC current with different calculation methods.

The inductance at no load and full load (300A) conditions calculated from the 3D real winding model is:

L_{noload} [µH]	L_{300A} [µH]
51.36	38.59

4.7 – Conclusions

In this chapter an introduction to finite element method is made. A sensibility study of the core's geometric dimensions influence on the inductor losses is conducted.

The possible configurations were ranked based on weights obtained from the sensibility study. The better configurations per material were simulated on Ansys Maxwell and the decision about the core's geometric dimensions was made.

After the core is chosen the winding design takes place. A comparison between the litz and solid wire configurations is done. For this specific application, the solid wire has

approximately 20% higher winding losses but has lower cost. For this reason solid wire is the final option for this inductor.

The four different FEA models and the analytical calculation showed very similar results which are a good indication for the inductor to be built.

Chapter 5

Inductor Building and Test Methods

This chapter deals with the building by hand of the inductor and introduces methods on how to measure its inductance and power losses during the DC-DC converter operation.

5.1 – Building the inductor

The inductor's core is composed by two toroidal High Flux cores that attached to each other with hot glue. The winding consists of 9 parallel branches, each with 19 turns around the core, with a margin of 25% on length which results in approximately 45 meters of copper wire, leaving each branch with a length close to 5 meters.

A base with an adaptive clamp tool and a semi circumference cut with the interior diameter of the core has been developed, see Figure 5.1. This was probably the object that made this winding by hand possible. This is because the 3.5mm copper wire is not easy to bend around the core. A wooden mallet was used to help bending the wire without injuring the copper insolation. The final inductor and the fast charger components are shown in Figure 5.2.

(a)

(b)

Figure 5.1 – Base with clamp tool used to wind the inductor: (a) top view, (b) front view.

Because the parasitic capacitances weren't calculated during the design stage, the QuadTech 1920 Precision LCR meter was used to confirm that with the increase in frequency the capacitive component don't grow enough to cause problems and also to confirm that the core's permeability remains constant for the frequency range of the DC-DC converter. The results are shown on Figure 5.3, it's possible to conclude that the effect of frequency on the inductance can be neglected for the fast charger operating conditions. The value of inductance obtained at no load conditions for the frequency range tested is around 48µH, which is inside the expected interval $51.4\ \mu H \pm 8\%$.

(a) (b)

Figure 5.2 – (a) Built inductor, (b) Fast charger components.

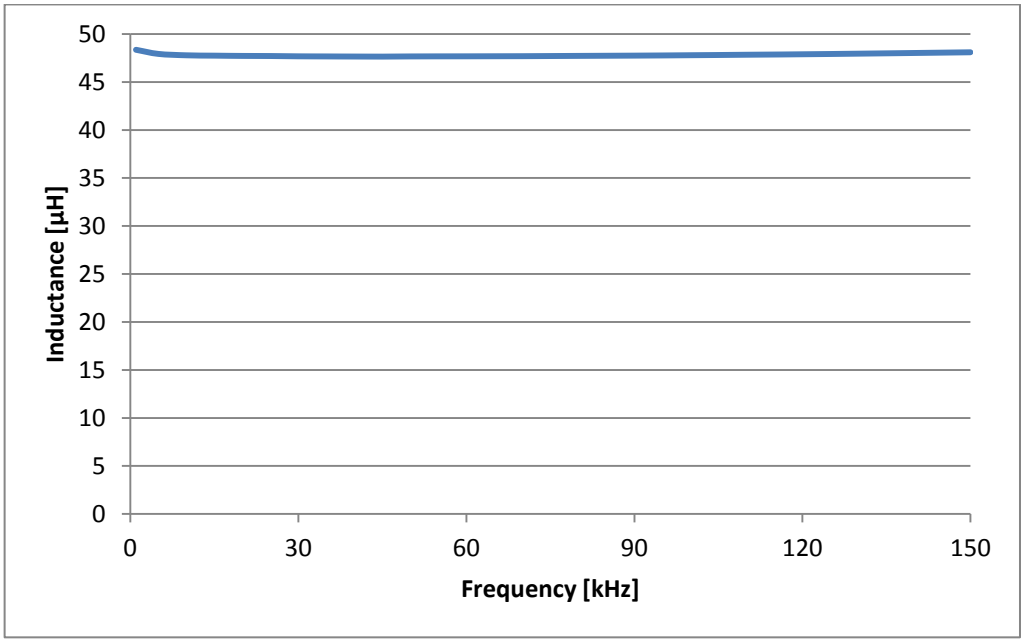

Figure 5.3 – Inductance vs Frequency at no load conditions.

5.2 – Inductance Measurement

Depending on the inductor's final application there are different methods to measure inductance [44]. The method used in this thesis was adapted from the proposed method in [45]. This method measures the inductance during operation of the DC-DC converter without requiring LCR meters.

Using a differential probe of an oscilloscope and a current clamp to measure inductor's voltage and current during fast charger operation, the waveforms seen will be similar to the ones on Figure 5.4. It's possible to see on the figure that while the inductor current is rising (point B to C), the inductor's voltage is increasing slightly. Since the slope of the current is constant (from B to C), the increase in the inductor voltage will occur due to the resistance of the winding. The calculation of inductance is done on the instant where the slope of the current changes abruptly (A to B or C to D) which produces a step on the inductors voltage due to the inductance value. The winding resistance and the inductance are calculated by (5.1) and (5.2) respectively.

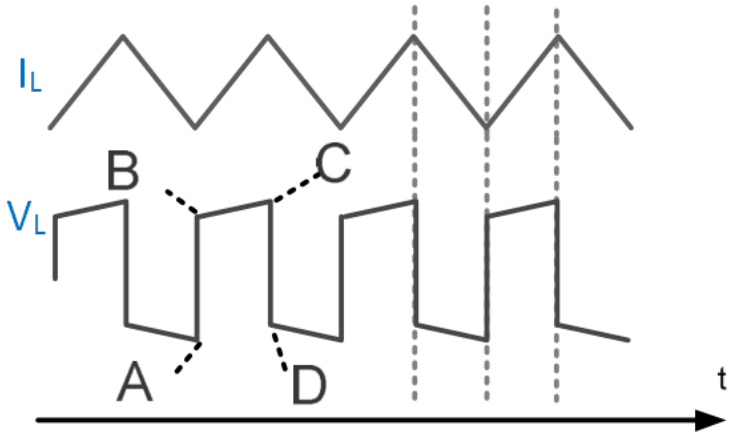

Figure 5.4 – Typical BDC inductor's current and voltage waveforms, edited from [45].

$$R_{winding} = \frac{V_L(\mathrm{C}) - V_L(\mathrm{B})}{i_L(C) - i_L(\mathrm{B})} \tag{5.1}$$

$$L = \frac{V_L(\mathrm{B}) - \mathrm{V}_L(A)}{2\,di_L/dt} \tag{5.2}$$

5.3 – Inductor Losses Measurement

One way to measure the inductor losses is to put the inductor under test in a thermal isolated chamber and measure the temperature difference between the inlet and outlet coolant. This method is universal but very time consuming [46]. For this reason in this thesis it's preferred the method utilized in [47] and [48] where an open secondary winding is added to the inductor and its voltage is monitored. The inductor core losses are calculated by (5.3), where N_1 is the original number of turns of the inductor, N_2 is the number of turns of the open secondary winding and v_2 is the measured voltage of the secondary winding.

$$P_{core} = f \int_0^T \frac{N_1}{N_2} v_2(t)\, i_L(t)\, dt \tag{5.3}$$

The winding losses are calculated using (5.4), noting that the winding resistance is measured by the method introduced in the previous section.

$$P_{winding} = \frac{1}{T} \int_0^T R_{winding} i_L(t)^2\, dt \tag{5.4}$$

5.4 – Conclusions

This chapter was reserved for documenting the process of building the inductor and for introducing methods to perform important measurements, specific to the DC-DC converter operation, that can validate the results obtained on Chapter 4.

Chapter 6

Conclusions

6.1 – Final considerations

In this thesis an inductor for an EV fast charger is designed and built. This design included a study of the fast charger which uses SiC MOSFETs in order to reach higher frequencies decreasing the size of the overall system while maintaining good efficiency. It also included a detailed study of the inductor in order not only to guarantee the requisites of the fast charger but also a good performance with an acceptable cost and size.

The study of the fast charger included a mathematical and a numerical simulation model. The first is built to analytically obtain the value of inductance required, the output power of the converter and the operating condition that maximizes the switching frequency, while the numerical simulation model is used to validate the output results of the mathematical model.

The inductor design is made in four steps:

1. First a review of the existent core materials in the market is performed, and then the choice of the materials and shapes considered better suited for the application is made taking into account practical applications already built and studies comparing cost, sizes and efficiency existent in the literature.
2. A sensibility study using software based on FEM is performed with the objective of understanding the effect of the core geometry dimensions on the inductor losses for similar values of inductance on the different core materials included in the study. A ranking of the cores configurations existent in the market is done which gives as output the better configurations per material. FEA is performed to decide the best of the available core configurations.
3. The winding design is made comparing the best configurations achieved using solid and Litz wire. The final decision took into account the excess in losses and cost for the both types of wire.

4. A thermal verification is performed in order to confirm that the designed inductor doesn't reach temperatures higher than the limits supported by the core material and the wire isolation.

The designed inductor is made of 19 turns replicated in 9 parallel branches of 3.5mm solid wire, two cores with an OD of 132.6mm made from High Flux with a relative permeability of 26. Under simulations, the results are satisfactory maintaining approximately 38.6µH at 300A from an initial 51.4µH of inductance value, while increasing its temperature by around 90^{o}C in respect to the ambient temperature, due to the approximately 160W of losses at 120^{o}C.

6.2 – Future perspectives

The inductor design method proposed in this thesis could be complemented with a thermal sensibility study using FEA that would take into account the core size and shape, window fill factor, material thermal properties, cooling method and mounting conditions to predict accurately the convection and radiation heat transfer coefficients. This would simplify the temperature rise calculation when a more detailed study is needed.

Also interesting would be to create a stage on the design strategy that would calculate the inductor parasitic capacitances and study its impact on the inductor and converter performance.

A more complete study of the fast charger that would consider a variable current ripple for different values of LV to HV ratio (k) could result in a smaller inductor and an overall more efficient converter due to the resulting lower switching frequency without the need of a bigger inductor.

Bibliography

[1] "Ansys Maxwell V16 Training Manual: Maxwell Transient Solvers." Ansys Inc., pp. 1–24, 2013.

[2] M. S. Rylko, B. J. Lyons, J. G. Hayes, and M. G. Egan, "Revised magnetics performance factors and experimental comparison of high-flux materials for high-current dc-dc inductors," *IEEE Trans. Power Electron.*, vol. 26, no. 8, pp. 2112–2126, 2011.

[3] T. Ishimine, A. Watanabe, T. Ueno, T. Maeda, and T. Tokuoka, "Development of low-iron-loss powder magnetic core material for high-frequency applications," *SEI Tech. Rev.*, no. 72, pp. 117–123, 2011.

[4] G. L. Johnson, *Solid State Tesla Coil*. Manhattan, 2001.

[5] A. van den Bossche and V. C. Valchev, *Inductors and Transformers for Power Electronics*. CRC Press, 2005.

[6] W. a. Roshen, "Fringing field formulas and winding loss due to an air gap," *IEEE Trans. Magn.*, vol. 43, no. 8, pp. 3387–3394, 2007.

[7] W. a. Roshen, "High-frequency fringing fields loss in thick rectangular and round wire windings," *IEEE Trans. Magn.*, vol. 44, no. 10, pp. 2396–2401, 2008.

[8] W. Lundquist, "Minimize Winding Losses in High-Frequency Inductors," *Power Electronics Technology*, no. July, pp. 14–18, 2008.

[9] L. H. Dixon, "Windings," in *TI Magnetics Design Handbook*, Texas Instruments, 2001, p. Topic 3.

[10] M. Sippola, "Developments for the high frequency power transformer design and implementation," Ph.D. dissertation, Helsinki University of Technology Applied Electronics Laboratory, 2003.

[11] W. G. Hurley, E. Gath, and J. G. Breslin, "Optimizing the AC resistance of multilayer transformer windings with arbitrary current waveforms," *IEEE Trans. Power Electron.*, vol. 15, no. 2, pp. 369–376, 2000.

[12] M. S. Ryłko, B. J. Lyons, K. J. Hartnett, J. G. Hayes, and M. G. Egan, "Magnetic material comparisons for high-current gapped and gapless foil wound inductors in high frequency DC-DC converters," *2008 13th Int. Power Electron. Motion Control Conf. EPE-PEMC 2008*, pp. 1249–1256, 2008.

[13] H. Skarrie, “Design of Powder Core Inductors,” Licentiate Thesis, Lund University, 2001.

[14] M. Leibl and J. W. Kolar, “Comparative Analysis of Inductor Concepts for High Peak Load Low Duty Cycle Operation Comparative Analysis of Inductor Concepts for High Peak Load Low Duty Cycle Operation,” vol. V, no. Ipec, pp. 899–906, 2014.

[15] M. S. Rylko, K. J. Jarnett, J. G. Hayes, and M. G. Egan, “Magnetic Material Selection for High Power High Frequency Inductors in DC-DC Converters,” *Twenty-Fourth Annu. IEEE Appl. Power Electron. Conf. Expo. 2009. APEC 2009.*, pp. 2043–2049, 2009.

[16] J. K. Fredrik Rosén, “Powder Material for Inductor Cores: Evaluation of MPP, Sendust and High flux core charactristics,” MSc. Thesis, Chalmers University of Technology - Department of Energy and Environment, 2013.

[17] M. Rylko, “Magnetic Materials and Soft-Switched Topologies for High-Current DC-DC Converters,” Ph.D. Thesis, University College Cork, 2011.

[18] B. G. You, J. S. Kim, B. K. Lee, G. B. Choi, and D. W. Yoo, “Optimization of powder core inductors of buck-boost converters for hybrid electric vehicles,” *J. Electr. Eng. Technol.*, vol. 6, no. 4, pp. 527–534, 2011.

[19] A. Goldman, *Magnetic Components for Power Electronics*. Kluwer Academic Publishers, 2002.

[20] B. York, “Inductor Design – with Continous/DC Current.”

[21] (Magnetics Inc.), “Magnetic Cores for Switching Power Supplies,” 1999.

[22] J. J. W. Kolar, U. Drofenik, J. Biela, M. L. Heldwein, H. Ertl, T. Friedli, and S. D. Round, “PWM converter power density barriers,” *Power Convers. Conf. - Nagoya*, vol. L, 2007.

[23] H. R. Karshenas, H. Daneshpajooh, A. Safaee, P. Jain, and A. Bakhshai, “Bidirectional DC-DC Converters for Energy Storage Systems, Energy Storage in Emerging Era of Smart Grids,” 2011.

[24] B. J. Lyons, J. G. Hayes, and M. G. Egan, “Magnetic material comparisons for high-current inductors in low-medium frequency DC-DC converters,” *Conf. Proc. - IEEE Appl. Power Electron. Conf. Expo. - APEC*, pp. 71–77, 2007.

[25] Y. Chen, H. Z. De La Parra, and F. Hess, “Dynamic simulation of EV fast charging with integration of renewables,” *2012 IEEE Int. Electr. Veh. Conf. IEVC 2012*, pp. 1–5, 2012.

[26] G. Mauri and A. Valsecchi, “The role of Fast Charging Stations for Electric Vehicles in the integration and optimization of distribution grid with renewable energy sources,” 2012.

[27] B. Ozpineci and L. Tolbert, “Smaller, faster, tougher,” *IEEE Spectr.*, vol. 48, no. 10, 2011.

[28] J. K. Reed, J. McFarland, J. Tangudu, E. Vinot, R. Trigui, G. Venkataramanan, S. Gupta, and T. Jahns, “Modeling power semiconductor losses in HEV powertrains using Si and SiC devices,” *2010 IEEE Veh. Power Propuls. Conf. VPPC 2010*, 2010.

[29] T. E. Salem, D. P. Urciuoli, V. Lubomirsky, and G. K. Ovrebo, “Design considerations for high power inductors in DC-DC converters,” *IEEE*, pp. 1258–1263, 2007.

[30] B. G. You, B. K. Lee, S. W. Lee, G. B. Choi, and D. W. Yoo, “Experimental comparison of mega flux and JNEX inductors in high power dc-dc converter of hybrid electric vehicles,” *2011 IEEE Veh. Power Propuls. Conf. VPPC 2011*, 2011.

[31] M. Greconici, “Some Examples that Use the FEM in PM Generators Analysis,” *Electron. ETF*, vol. 16, no. 1, pp. 32–36, 2012.

[32] J. P. A. Bastos and S. Nelson, *Electromagnetic Modeling by Finite Element Methods*. Marcel Dekker, Inc., 2003.

[33] G. Meunier, *The Finite Element Method for Electromagnetic Modeling*. John Wiley & Sons, Inc., 2008.

[34] Z. L. Gaing, Q. Q. Wang, and J. A. Chiang, “Optimization of in-wheel PM motor by fuzzy-based Taguchi method,” *2010 Int. Power Electron. Conf. - ECCE Asia -, IPEC 2010*, vol. 821, pp. 1312–1316, 2010.

[35] R. A. Salas and J. Pleite, “Simple Procedure to Compute the Inductance of a Toroidal Ferrite Core from the Linear to the Saturation Regions,” pp. 2452–2463, 2013.

[36] R. A. Salas and J. Pleite, “Simulation of waveforms of a ferrite inductor with saturation and power losses,” *Materials (Basel).*, vol. 7, no. 3, pp. 1850–1865, 2014.

[37] D. C. Montgomery, *Design and analysis of experiments*, Fifth edit. John Wiley & Sons, Inc., 2008.

[38] A. Dolan and F. Stefanescu, “Optimization of Modular Toroid Coil Geometry of a Superconducting Magnetic Energy Storage Device Using Design of Experiments and FEM,” *IEEE*, 2014.

[39] Y. Gu and D. Jin, “Drop test simulation and DOE analysis for design optimization of microelectronics packages,” in *Electronic Components and Technology Conference*, 2006, vol. 2006, pp. 422–427.

[40] D. C. Montgomery and G. C. Runger, *Applied Statistics and Probability for Engineers*, Third edit. John Wiley & Sons, Inc., 2003.

[41] M. Zdanowski, J. Rabkowski, K. Kostov, R. Barlik, and H. P. Nee, “Design and evaluation of reduced self-capacitance inductor for fast-switching SiC BJT dc/dc

converters," *15th Int. Power Electron. Motion Control Conf. Expo. EPE-PEMC 2012 ECCE Eur.*, pp. 1–7, 2012.

[42] C. R. Sullivan and R. Y. Zhang, "Simplified Design Method for Litz Wire," pp. 2667–2674, 2014.

[43] W. Lundquist, V. Yang, and C. Castro, "Low AC Resistance Foil Inductor," pp. 1–5.

[44] J. Schliewe, S. Schefler, and S. Weber, "Simulating Saturation Behavior of Inductive Components," no. May, 2014.

[45] T. Liu, C. Fu, S. Ozev, and B. Bakkaloglu, "A Built-In Self-Test Technique for Load Inductance and Lossless Current Sensing of DC-DC Converters," *IEEE Comput. Soc.*, 2014.

[46] M. Mu and F. C. Lee, "A new high frequency inductor loss measurement method," *IEEE Energy Convers. Congr. Expo.*, pp. 1801–1806, 2011.

[47] J. Mühlethaler, J. Biela, J. W. Kolar, and A. Ecklebe, "Core losses under the DC bias condition based on steinmetz parameters," *IEEE Trans. Power Electron.*, vol. 27, no. 2, pp. 953–963, 2012.

[48] A. Hilal, S. Member, M. Raulet, C. Martin, and F. Sixdenier, "Power Loss Prediction and Precise Modeling of Magnetic Powder Components in DC-DC Power Converter Application," *IEEE Trans. Power Electron.*, vol. 8993, no. c, pp. 1–1, 2014.

Appendix A

Powder Material Curves

A.1 – MPP

In this section are presented the magnetic characteristic curves of the MPP materials included in the sensibility study. On Figure A.1 is presented the core selector chart for these materials. Figure A.2 presents the permeability vs DC bias characteristic for the different relative magnetic permeabilities of MPP. Table A.1 indicates the analytic expression that originates the curves from Figure A.2. The core loss density curves for MPP 14µ and 26µ are given on Figure A.3 and Figure A.4 respectively.

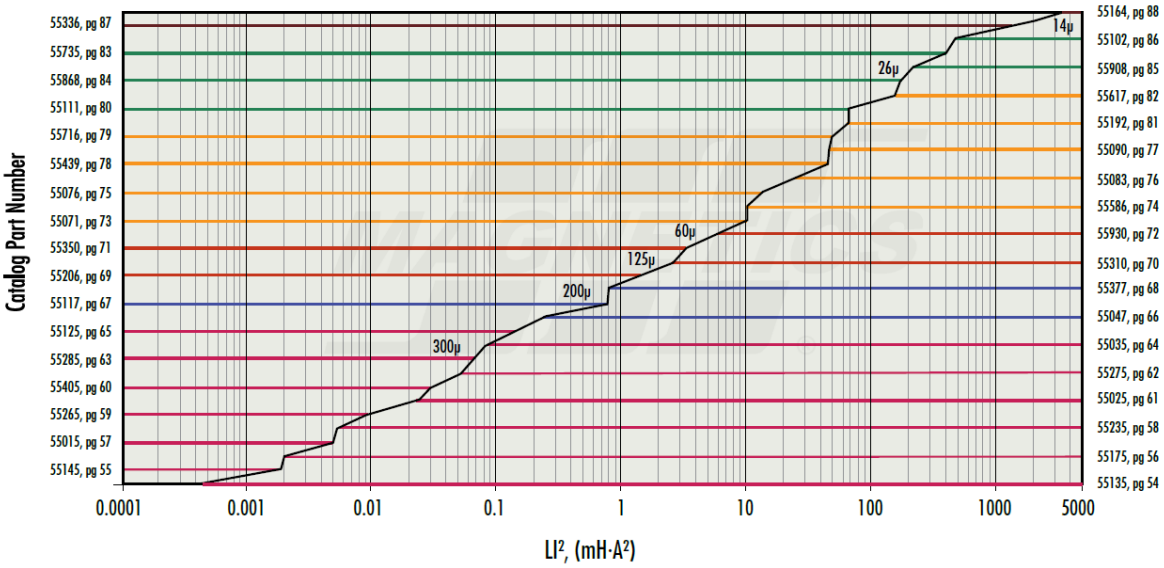

Figure A.1 – MPP core selector chart.

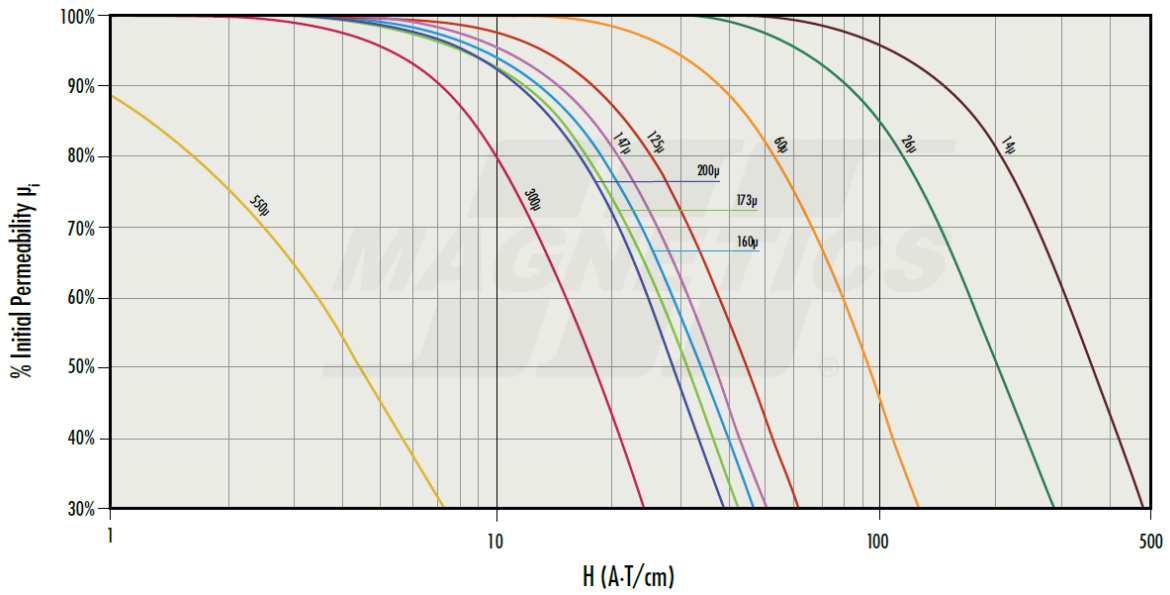

Figure A.2 – MPP Permeability vs DC bias curves.

Table A.1 – Analytic expression and its parameters for the MPP permeability vs DC bias curves.

$$\mu_{eff}/\mu_i = a + bH + cH^2 + dH^3 + eH^4 \qquad , H \text{ in } A/cm$$

Material	μ_i	a	b	c	d	e
MPP	14	9.985×10^{-1}	4.257×10^{-4}	-9.611×10^{-6}	1.491×10^{-8}	-6.250×10^{-12}
	26	9.985×10^{-1}	1.142×10^{-3}	-3.762×10^{-5}	1.222×10^{-7}	-1.218×10^{-10}

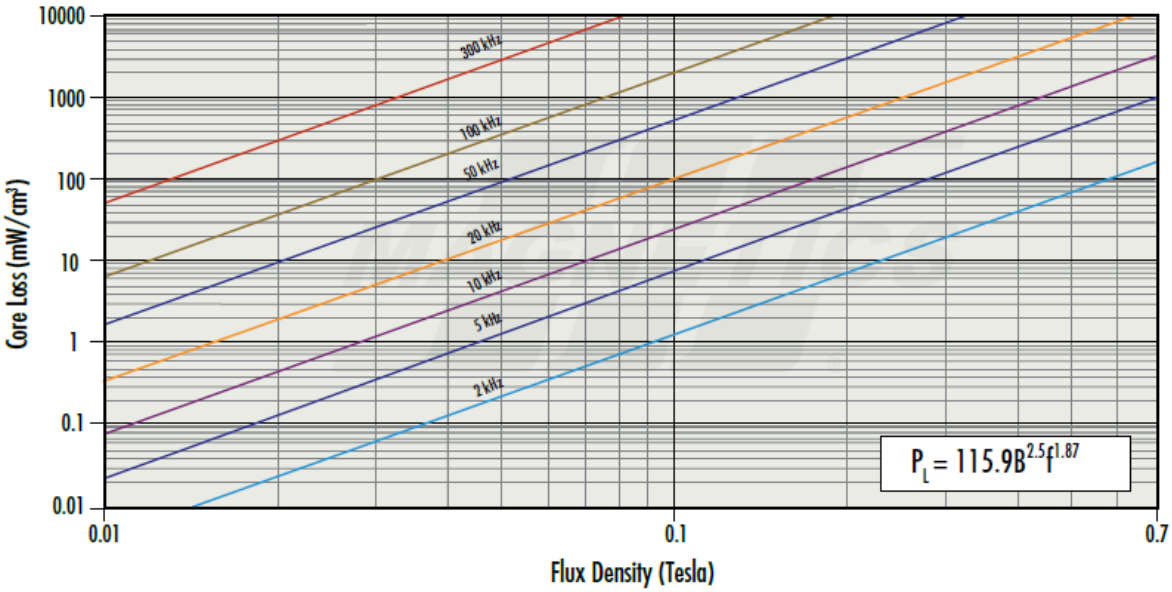

Figure A.3 – MPP 14µ core loss density curves.

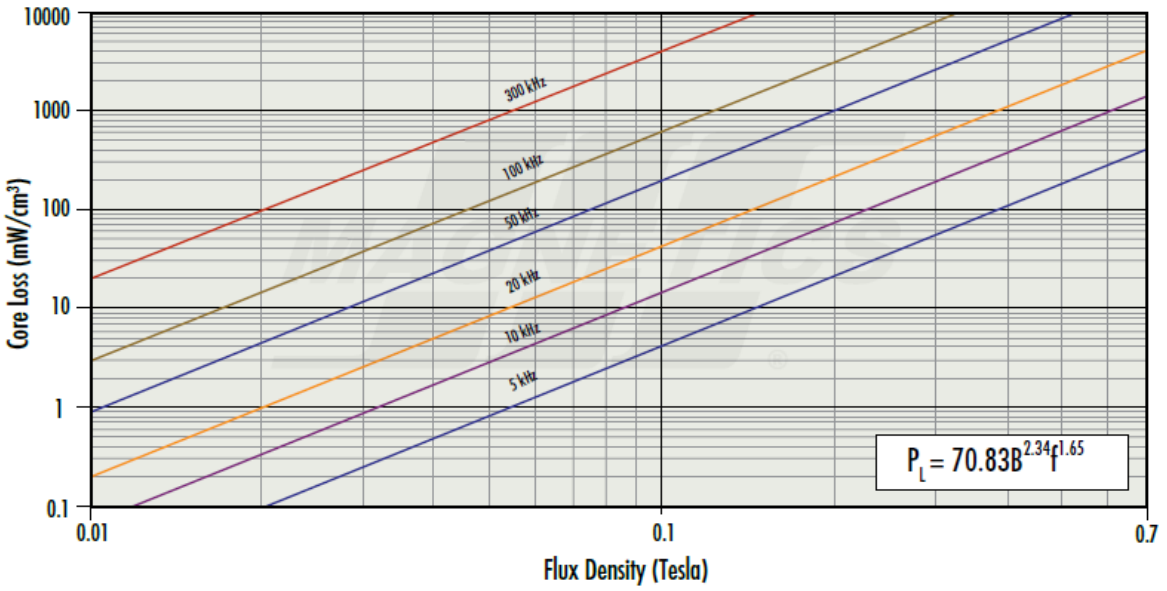

Figure A.4 – MPP 26µ core loss density curves.

A.2 – High Flux

In this section are presented the magnetic characteristic curves of the High Flux materials included in the sensibility study. On Figure A.5 is presented the core selector chart for these materials. Figure A.6 presents the permeability vs DC bias characteristic for the different relative magnetic permeabilities of High Flux. Table A.2 indicates the analytic expression that originates the curves from Figure A.6. The core loss density curves for High Flux 14µ and 26µ are given on Figure A.7 and Figure A.8 respectively.

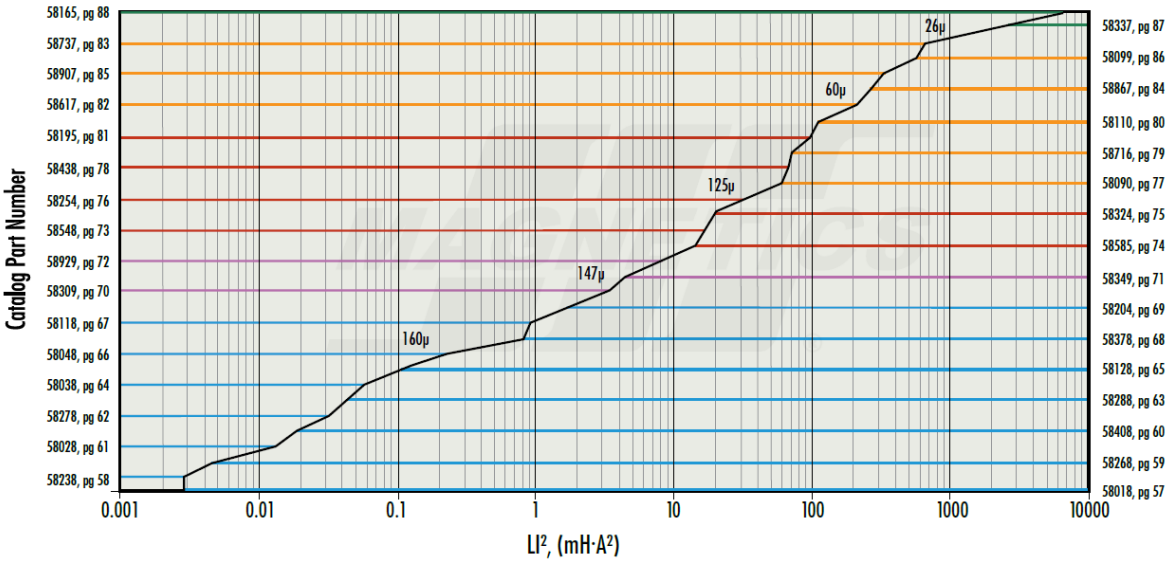

Figure A.5 – High Flux core selector chart.

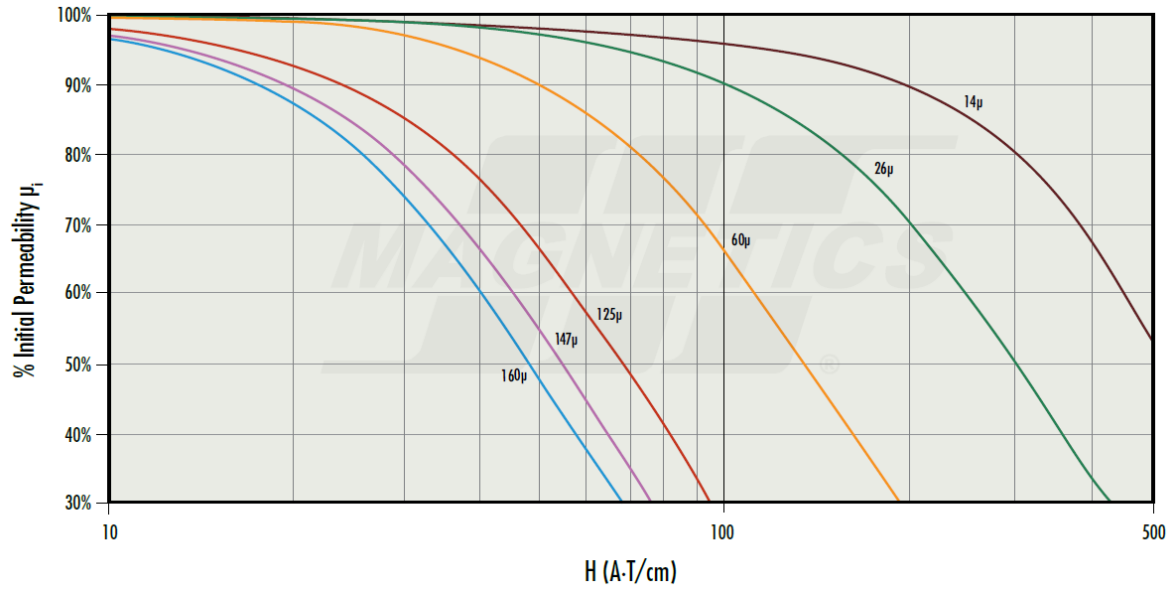

Figure A.6 – High Flux Permeability vs DC bias curves.

Table A.2 - Analytic expression and its parameters for the High Flux permeability vs DC bias

$\mu_{eff}/\mu_i = a + bH + cH^2 + dH^3 + eH^4 \quad , H \text{ in } A/cm$						
Material	μ_i	a	b	c	d	e
High Flux	14	1	-3.954×10^{-4}	4.270×10^{-7}	-6.515×10^{-9}	6.938×10^{-12}
	26	1	-8.078×10^{-5}	-1.111×10^{-5}	2.344×10^{-8}	-1.392×10^{-11}

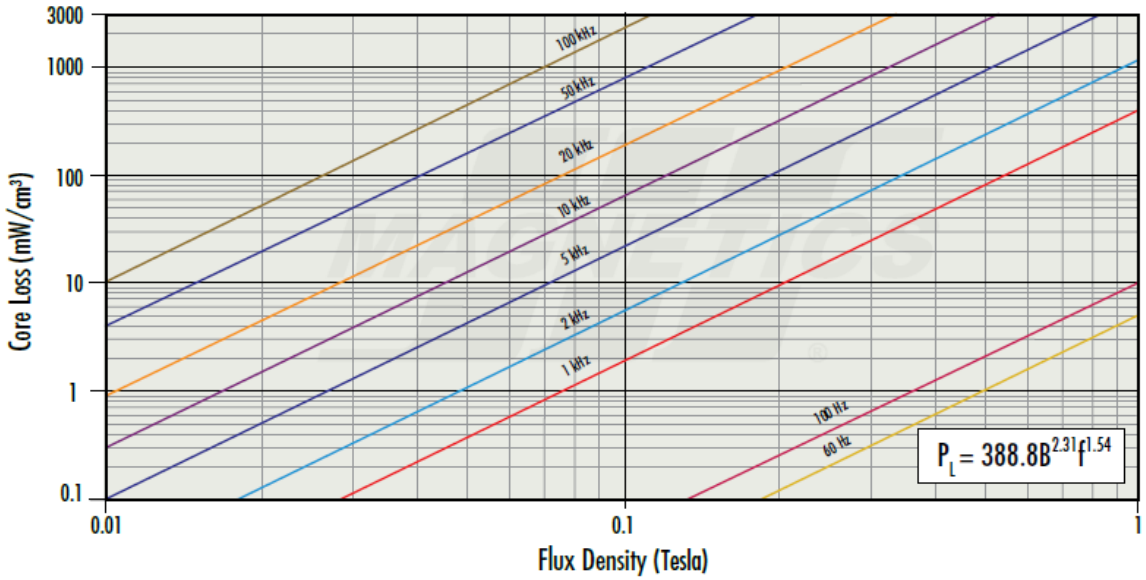

Figure A.7 – High Flux 14µ core loss density curves.

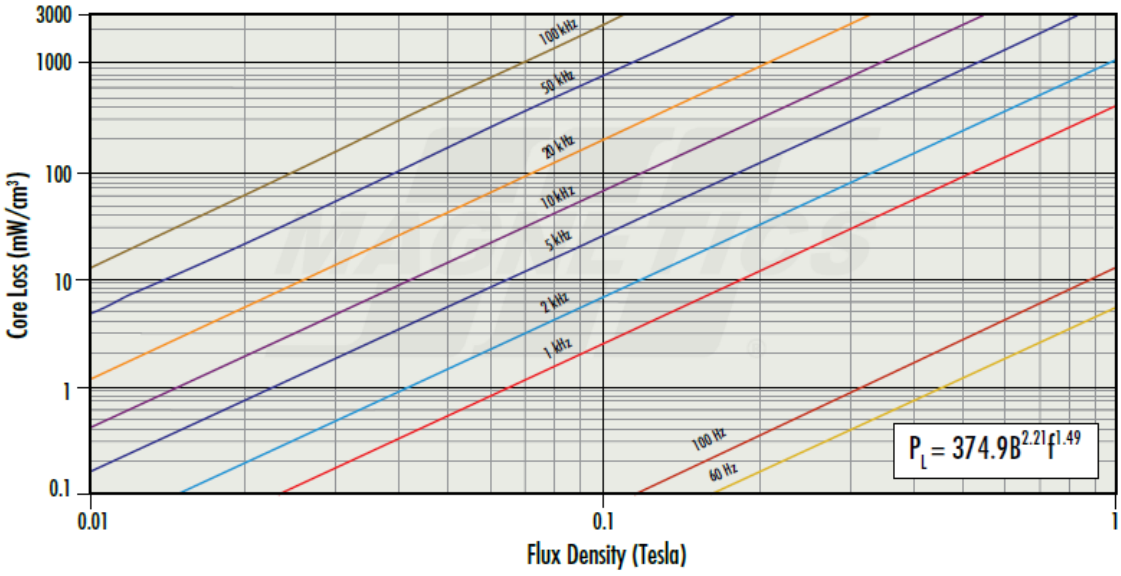

Figure A.8 – High Flux 26µ core loss density curves.

A.3 – Kool Mu

In this section are presented the magnetic characteristic curves of the material Kool Mu included in the sensibility study. On Figure A.9 is presented the core selector chart for these materials. Figure A.10 presents the permeability vs DC bias characteristic for the different relative magnetic permeabilities of Kool Mu. Table A.3 indicates the analytic expression that originates the curves from Figure A.10. The core loss density curves for Kool Mu 26µ are given on Figure A.11.

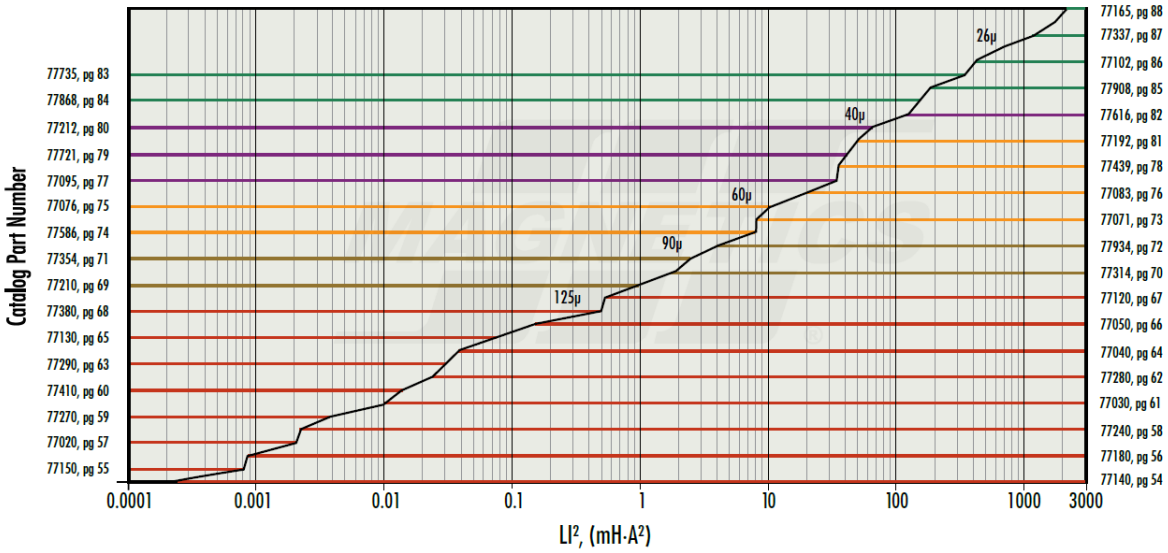

Figure A.9 – Kool Mu core selector chart.

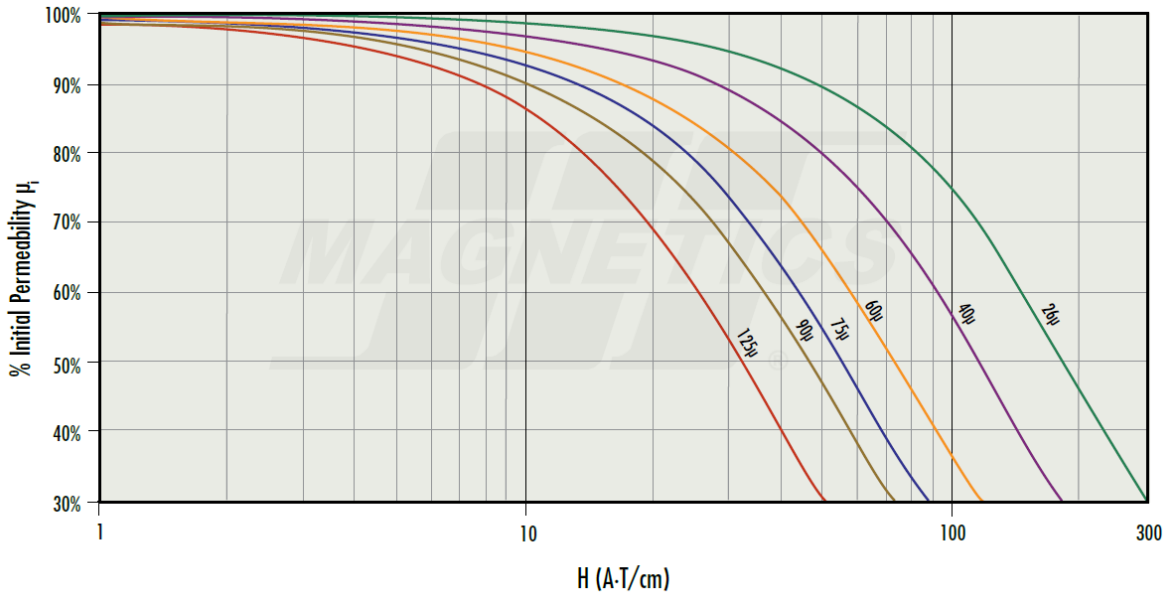

Figure A.10 – Kool Mu Permeability vs DC bias curves.

Table A.3 - Analytic expression and its parameters for the Kool Mu permeability vs DC bias

$$\mu_{eff} / \mu_i = a + bH + cH^2 + dH^3 + eH^4 \qquad , H \text{ in } A/cm$$

Material	μ_i	a	b	c	d	e
Kool Mu	26	1	-1.248×10^{-3}	-2.020×10^{-5}	8.354×10^{-8}	-9.503×10^{-11}

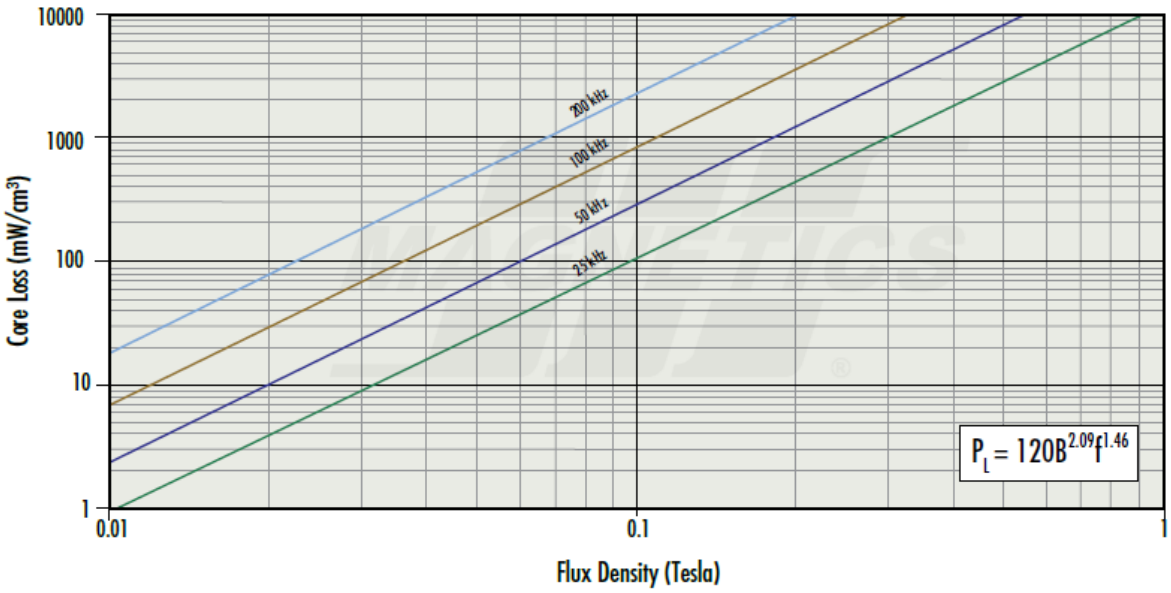

Figure A.11 – Kool Mu 26µ core loss density curves.

Appendix B

Sensibility Study Results

B.1 – DoE planning

In this section the total configurations to be simulated by FEA, with their geometric dimensions, are presented.

Table B.1 – MPP DoE FEA input table.

	DoE Parameters		Ansys Maxwell Inputs				
Run	**Cross Section Area**	**Magnetic Length**	**IR**	**OR**	**HT**	**N**	**Material**
1	15	24,3	29,4	49,7	73,9	23	MPP 14µ
2	15	32,4	39,2	66,3	55,4	24	
3	15	41,2	49,9	84,3	43,6	26	
4	30	24,3	29,4	49,7	147,8	14	
5	30	32,4	39,2	66,3	110,7	16	
6	30	41,2	49,9	84,3	87,2	18	
7	50	24,3	29,4	49,7	246,3	11	
8	50	32,4	39,2	66,3	184,5	12	
9	50	41,2	49,9	84,3	145,3	14	
10	15	24,3	29,4	49,7	73,9	20	MPP 26µ
11	15	32,4	39,2	66,3	55,4	23	
12	15	41,2	49,9	84,3	43,6	22	
13	30	24,3	29,4	49,7	147,8	12	
14	30	32,4	39,2	66,3	110,7	13	
15	30	41,2	49,9	84,3	87,2	14	
16	50	24,3	29,4	49,7	246,3	8	
17	50	32,4	39,2	66,3	184,5	9	
18	50	41,2	49,9	84,3	145,3	10	

Table B.2 – High Flux and Kool Mu DoE FEA input table

	DoE Parameters		Ansys Maxwell Inputs				
Run	**Cross Section Area**	**Magnetic Length**	**IR**	**OR**	**HT**	**N**	**Material**
19	15	24,3	29,4	49,7	73,9	20	High Flux 14µ
20	15	32,4	39,2	66,3	55,4	22	
21	15	41,2	49,9	84,3	43,6	25	
22	30	24,3	29,4	49,7	147,8	14	
23	30	32,4	39,2	66,3	110,7	16	
24	30	41,2	49,9	84,3	87,2	18	
25	50	24,3	29,4	49,7	246,3	11	
26	50	32,4	39,2	66,3	184,5	12	
27	50	41,2	49,9	84,3	145,3	14	
28	15	24,3	29,4	49,7	73,9	16	High Flux 26µ
29	15	32,4	39,2	66,3	55,4	18	
30	15	41,2	49,9	84,3	43,6	19	
31	30	24,3	29,4	49,7	147,8	11	
32	30	32,4	39,2	66,3	110,7	12	
33	30	41,2	49,9	84,3	87,2	13	
34	50	24,3	29,4	49,7	246,3	8	
35	50	32,4	39,2	66,3	184,5	9	
36	50	41,2	49,9	84,3	145,3	10	
37	15	24,3	29,4	49,7	73,9	25	Kool Mu 26µ
38	15	32,4	39,2	66,3	55,4	24	
39	15	41,2	49,9	84,3	43,6	24	
40	30	24,3	29,4	49,7	147,8	13	
41	30	32,4	39,2	66,3	110,7	14	
42	30	41,2	49,9	84,3	87,2	15	
43	50	24,3	29,4	49,7	246,3	9	
44	50	32,4	39,2	66,3	184,5	10	
45	50	41,2	49,9	84,3	145,3	11	

B.2 – DoE Results

In this section are presented the totality of the DoE FEA results.

Table B.3 – MPP DoE FEA Results.

Run	Material	$L_{no\ load}$ [µH]	L_{load} [µH]	Core Losses [W]	Copper Losses [W]	Total Losses [W]
1	MPP 14µ	61,39	40,49	1,6	79,1	80,7
2		50,30	37,51	1,7	74,1	75,8
3		46,52	37,41	2,6	76,7	79,3
4		44,98	37,94	3,5	79,4	83,0
5		44,13	39,02	5,1	76,1	81,2
6		44,03	40,05	6,4	76,8	83,2
7		45,99	41,71	6,3	95,2	101,4
8		41,11	38,65	7,2	83,9	91,1
9		44,10	41,91	8,3	84,4	92,7
10	MPP 26µ	83,41	44,55	2,2	68,8	71,0
11		83,04	47,28	2,1	71,0	73,1
12		59,78	39,11	1,5	64,9	66,4
13		59,71	40,90	1,6	68,1	69,6
14		52,65	40,16	2,0	61,9	63,9
15		48,09	39,59	3,1	59,8	62,9
16		44,05	36,94	3,0	69,2	72,3
17		41,90	37,19	4,6	62,9	67,5
18		41,07	37,66	5,7	60,3	65,9

Table B.4 – High Flux and Kool Mu DoE FEA Results.

Run	Material	$L_{no\ load}$ [µH]	L_{load} [µH]	Core Losses [W]	Copper Losses [W]	Total Losses [W]
19	High Flux 14µ	46,98	39,78	10,4	68,8	79,1
20		42,79	37,98	13,5	67,9	81,4
21		43,52	39,42	15,8	73,7	89,6
22		45,56	41,69	17,4	79,4	96,9
23		44,69	41,60	19,0	76,1	95,1
24		44,60	41,98	19,9	76,8	96,7
25		46,58	43,79	20,4	95,2	115,6
26		41,65	39,69	19,1	83,9	103,0
27		44,67	42,76	20,6	84,4	105,0
28	High Flux 26µ	54,02	37,91	7,7	55,0	62,7
29		51,45	39,32	13,0	55,5	68,6
30		45,12	37,17	19,6	56,0	75,7
31		50,79	42,27	23,0	62,4	85,5
32		45,41	39,86	30,0	57,1	87,1
33		41,98	38,06	33,9	55,5	89,4
34		44,59	40,20	33,8	69,2	103,1
35		42,42	39,30	38,1	62,9	101,0
36		41,58	39,13	40,3	60,3	100,5
37	Kool Mu 26µ	131,50	50,27	2,1	86,0	88,1
38		91,32	41,77	1,6	74,1	75,7
39		71,91	38,14	1,4	70,8	72,2
40		70,78	39,97	1,5	73,8	75,3
41		61,67	39,85	2,5	66,6	69,1
42		55,79	39,57	4,5	64,0	68,5
43		56,33	39,86	4,3	77,9	82,2
44		52,24	40,05	7,0	69,9	76,9
45		49,96	40,29	9,6	66,3	75,9

B.3 – Analysis of results for MPP 14µ

In this section the statistical analysis of the MPP 14µ are presented. On Figure B.1 is presented the DoE FEA results for this specific material. On Table B.5 is given the mean performances for each parameter level. Figure B.2 presents the ANOVA table for this material and on Table B.6 it's given the parameters percentage contributions to inductor losses.

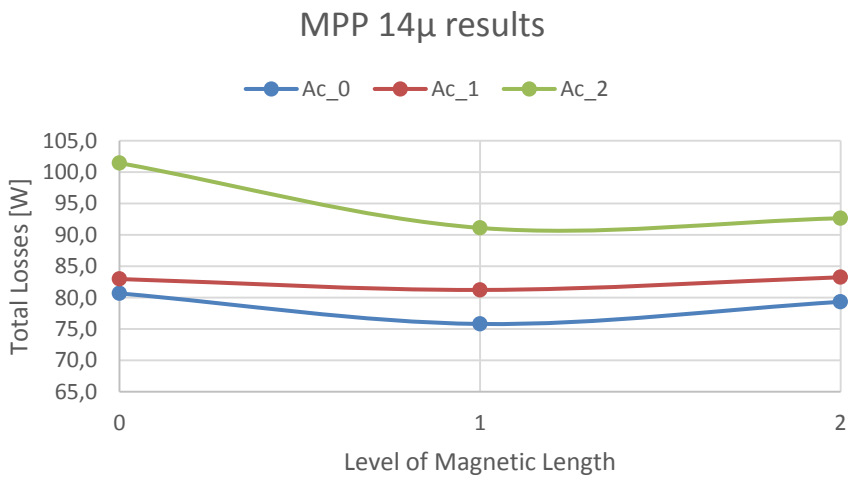

Figure B.1 – MPP 14µ DoE FEA results.

Table B.5 – MPP 14µ DoE mean inductor losses for each parameter level.

Parameters	Level	Mean Losses [W]
Cross Section	0	78,6
	1	82,5
	2	95,1
Magnetic Length	0	88,4
	1	82,7
	2	85,1

Analysis of Variance

Source	Sum Sq.	d.f.	Mean Sq.	F	Prob>F
Cross Section	445.217	2	222.609	30.73	0.0037
Magnetic Length	48.312	2	24.156	3.33	0.1405
Error	28.973	4	7.243		
Total	522.501	8			

Figure B.2 – MPP 14µ ANOVA table.

Table B.6 – MPP 14µ parameters Percentage Contribution.

Percentage Contribution	
Cross Section	85%
Magnetic Length	9%
Error	6%
total	100%

B.4 – Analysis of results for MPP 26µ

In this section the statistical analysis of the MPP 26µ are presented. On Figure B.3 is presented the DoE FEA results for this specific material. On Table B.7 is given the mean performances for each parameter level. Figure B.4 presents the ANOVA table for this material and on Table B.8 it's given the parameters percentage contributions to inductor losses.

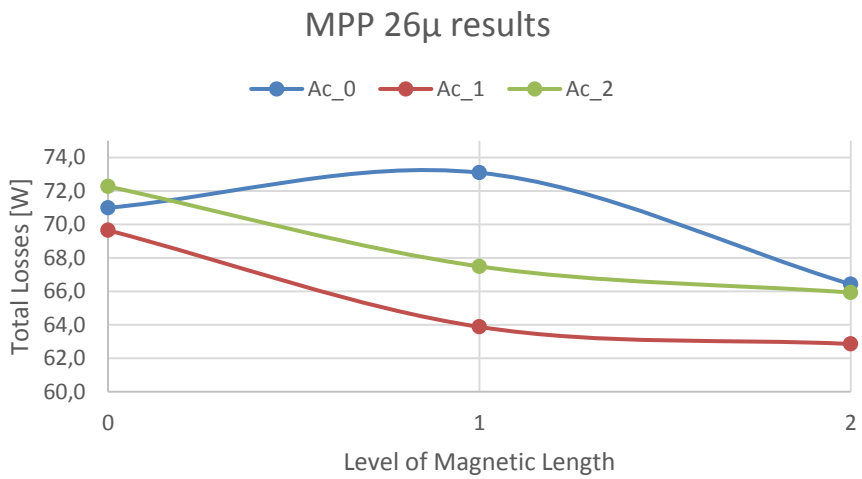

Figure B.3 - MPP 26µ DoE FEA results.

Table B.7 - MPP 26µ DoE mean inductor losses for each parameter level.

Parameters	Level	Mean Losses [W]
Cross Section	0	70,2
	1	65,5
	2	68,6
Magnetic Length	0	71,0
	1	68,2
	2	65,1

Analysis of Variance

Source	Sum Sq.	d.f.	Mean Sq.	F	Prob>F
Cross Section	34.405	2	17.2026	3.5	0.1322
Magnetic Length	52.318	2	26.1589	5.32	0.0746
Error	19.654	4	4.9135		
Total	106.377	8			

Figure B.4 - MPP 26µ ANOVA table.

Table B.8 - MPP 26µ parameters Percentage Contribution.

Percentage Contribution	
Cross Section	32%
Magnetic Length	49%
Error	18%
total	100%

B.5 – Analysis of results for High Flux 14µ

In this section the statistical analysis of the High Flux 14µ are presented. On Figure B.5 is presented the DoE FEA results for this specific material. On Table B.9 is given the mean performances for each parameter level. Figure B.6 presents the ANOVA table for this material and on Table B.10 it's given the parameters percentage contributions to inductor losses.

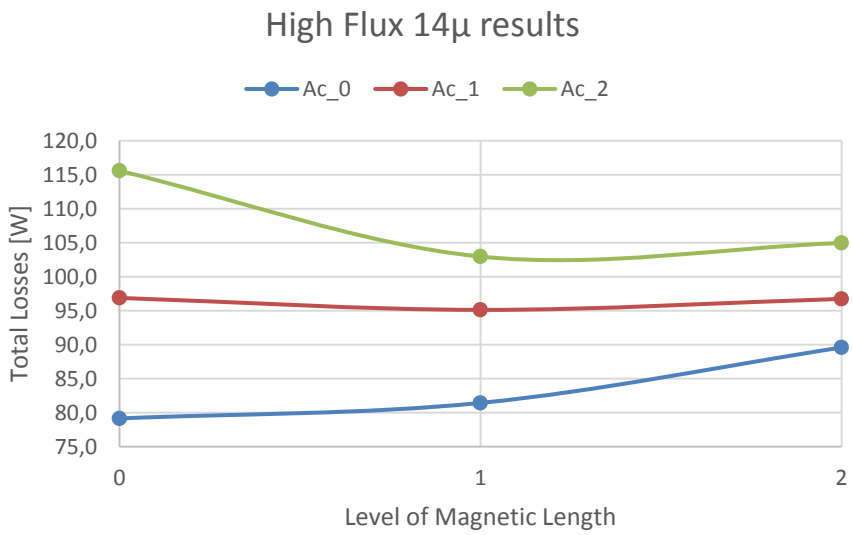

Figure B.5 – High Flux 14µ DoE FEA results.

Table B.9 – High Flux 14µ DoE mean inductor losses for each parameter level.

Parameters	Level	Mean Losses [W]
Cross Section	0	83,4
	1	96,2
	2	107,8
Magnetic Length	0	97,2
	1	93,2
	2	97,1

Analysis of Variance

Source	Sum Sq.	d.f.	Mean Sq.	F	Prob>F
Cross Section	897.97	2	448.983	14.67	0.0144
Magnetic Length	31.67	2	15.835	0.52	0.6312
Error	122.41	4	30.603		
Total	1052.05	8			

Figure B.6 – High Flux 14µ ANOVA table.

Table B.10 – High Flux 14µ parameters Percentage Contribution.

Percentage Contribution	
Cross Section	85%
Magnetic Length	3%
Error	12%
total	100%

B.6 – Analysis of results for High Flux 26µ

In this section the statistical analysis of the High Flux 26µ are presented. On Figure B.7 is presented the DoE FEA results for this specific material. On Table B.11 is given the mean performances for each parameter level. Figure B.8 presents the ANOVA table for this material and on Table B.12 it's given the parameters percentage contributions to inductor losses.

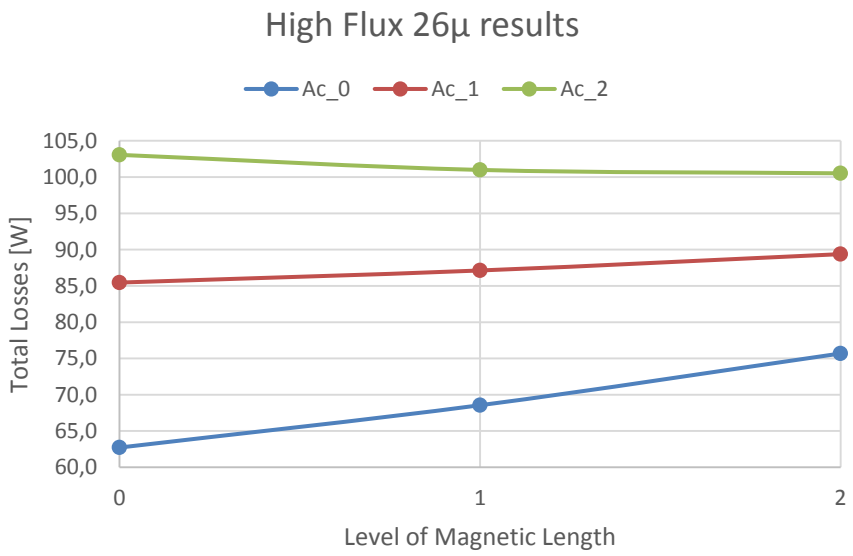

Figure B.7 – High Flux 26µ DoE FEA results.

Table B.11 – High Flux 26µ DoE mean inductor losses for each parameter level.

Parameters	Level	Mean Losses [W]
Cross Section	0	69,0
	1	87,3
	2	101,5
Magnetic Length	0	83,7
	1	85,6
	2	88,5

Analysis of Variance

Source	Sum Sq.	d.f.	Mean Sq.	F	Prob>F
Cross Section	1596.58	2	798.289	52.55	0.0013
Magnetic Length	34.95	2	17.474	1.15	0.403
Error	60.76	4	15.191		
Total	1692.29	8			

Figure B.8 – High Flux 26µ ANOVA table.

Table B.12 – High Flux 26µ parameters Percentage Contribution.

Percentage Contribution	
Cross Section	94%
Magnetic Length	2%
Error	4%
total	100%

B.7 – Analysis of results for Kool Mu 26µ

In this section the statistical analysis of the Kool Mu 26µ are presented. On Figure B.9 is presented the DoE FEA results for this specific material. On Table B.13 is given the mean performances for each parameter level. Figure B.10 presents the ANOVA table for this material and on Table B.14 it's given the parameters percentage contributions to inductor losses.

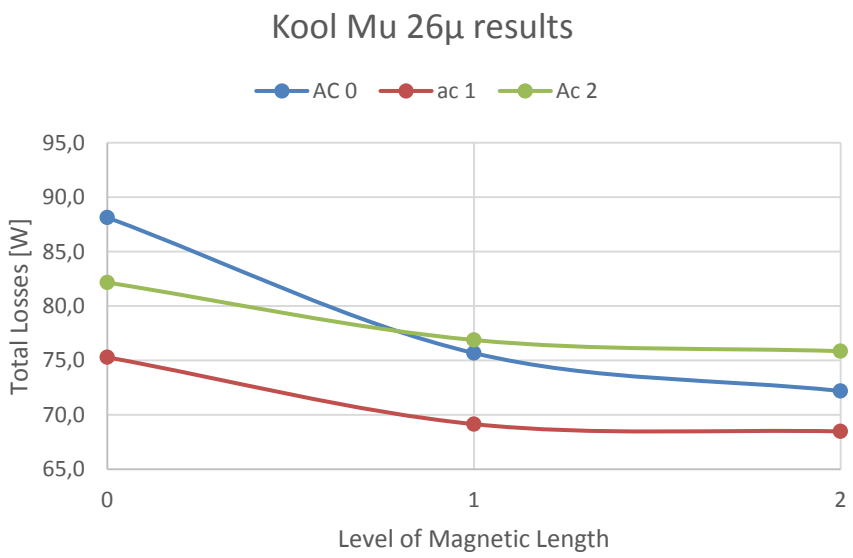

Figure B.9 – Kool Mu 26µ DoE FEA results.

Table B.13 – Kool Mu 26µ DoE mean inductor losses for each parameter level.

Parameters	Level	Mean Losses [W]
Cross Section	0	69,0
	1	87,3
	2	101,5
Magnetic Length	0	83,7
	1	85,6
	2	88,5

Analysis of Variance

Source	Sum Sq.	d.f.	Mean Sq.	F	Prob>F
Cross Section	113.01	2	56.5048	7.2	0.0472
Magnetic Length	160.114	2	80.0569	10.2	0.0269
Error	31.382	4	7.8455		
Total	304.505	8			

Figure B.10 – Kool Mu 26µ ANOVA table.

Table B.14 – Kool Mu 26µ parameters Percentage Contribution.

Percentage Contribution	
Cross Section	37%
Magnetic Length	53%
Error	10%
total	100%

Appendix C

Ranking of configurations

C.1 – Final Rankings

In this section are presented the rankings for all the core configurations considered.

MPP 14µ

Table C.1 – MPP 14µ Ranking of core configurations.

						Score		Weight of Saturation			
Material	Core ref.	Number of Cores	Number of Turns	Cross Section	Mag. Length	Saturation	Losses	0,2	0,25	0,3	0,35
MPP 14µ	OD165.1	1	35	9,87	41,2	69	89	85	84	83	82
	OD165.1	2	22	19,74	41,2	86	77	79	79	80	80
	OD165.1	3	18	29,61	41,2	91	65	70	72	73	74
	OD165.1	4	15	39,48	41,2	94	37	48	51	54	57
	OD165.1	5	14	49,35	41,2	94	7	25	29	33	38
	OD132.6	2	26	13,56	32,4	0	0	71	66	62	58
	OD132.6	3	20	20,34	32,4	82	80	81	81	81	81
	OD132.6	4	17	27,12	32,4	87	72	75	76	76	77
	OD132.6	5	15	33,9	32,4	90	57	63	65	67	68
	OD132.6	6	14	40,68	32,4	91	37	48	50	53	56
	OD132.6	7	13	47,46	32,4	92	17	32	36	39	43
	OD101.6	3	38	10,74	24,3	0	0	0	0	0	0
	OD101.6	4	24	14,32	24,3	0	0	0	0	0	0
	OD101.6	5	20	17,9	24,3	0	0	0	0	0	0
	OD101.6	6	18	21,48	24,3	0	0	0	0	0	0
	OD101.6	7	16	25,06	24,3	0	0	0	0	0	0
	OD101.6	8	15	28,64	24,3	0	0	0	0	0	0
	OD101.6	9	14	32,22	24,3	0	0	0	0	0	0
	OD101.6	10	13	35,8	24,3	0	0	0	0	0	0
	OD101.6	11	12	39,38	24,3	88	32	43	46	49	51
	OD101.6	12	12	42,96	24,3	88	21	34	38	41	45
	OD101.6	13	11	46,54	24,3	90	10	26	30	34	38

MPP 26µ

Table C.2 - MPP 26µ Ranking of core configurations.

						Score		Weight of Saturation			
Material	**Core ref.**	**Number of Cores**	**Number of Turns**	**Cross Section**	**Mag. Length**	**Saturation**	**Losses**	**0,2**	**0,25**	**0,3**	**0,35**
MPP 26µ	OD165.1	1	47	9,87	41,2	0	0	0	0	0	0
	OD165.1	2	18	19,74	41,2	73	66	67	67	68	68
	OD165.1	3	14	29,61	41,2	83	81	81	81	81	81
	OD165.1	4	12	39,48	41,2	87	74	77	77	78	79
	OD165.1	5	10	49,35	41,2	91	67	72	73	74	75
	OD132.6	2	28	13,56	32,4	0	0	0	0	0	0
	OD132.6	3	17	20,34	32,4	0	0	0	0	0	0
	OD132.6	4	13	27,12	32,4	76	51	56	58	59	60
	OD132.6	5	12	33,9	32,4	80	53	58	60	61	62
	OD132.6	6	11	40,68	32,4	83	48	55	56	58	60
	OD132.6	7	10	47,46	32,4	86	43	51	53	55	58
	OD101.6	3	28	10,74	24,3	0	0	0	0	0	0
	OD101.6	4	28	14,32	24,3	0	0	0	0	0	0
	OD101.6	5	22	17,9	24,3	0	0	0	0	0	0
	OD101.6	6	16	21,48	24,3	0	0	0	0	0	0
	OD101.6	7	13	25,06	24,3	0	0	0	0	0	0
	OD101.6	8	12	28,64	24,3	0	0	0	0	0	0
	OD101.6	9	11	32,22	24,3	0	0	0	0	0	0
	OD101.6	10	10	35,8	24,3	75	28	37	40	42	45
	OD101.6	11	10	39,38	24,3	75	25	35	38	40	43
	OD101.6	12	9	42,96	24,3	80	22	34	37	40	42
	OD101.6	13	9	46,54	24,3	80	20	32	35	38	41

High Flux 14µ

Table C.3 – High Flux 14µ Ranking of core configurations.

						Score		Weight of Saturation			
Material	Core ref.	Number of Cores	Number of Turns	Cross Section	Mag. Length	Saturation	Losses	0,2	0,25	0,3	0,35
High Flux 14µ	OD165.1	1	31	9,87	41,2	88	83	84	84	84	85
	OD165.1	2	22	19,74	41,2	93	59	65	67	69	70
	OD165.1	3	18	29,61	41,2	94	34	46	49	52	55
	OD165.1	4	15	39,48	41,2	95	18	33	37	41	45
	OD165.1	5	14	49,35	41,2	96	1	20	25	29	34
	OD132.6	2	24	13,56	32,4	0	0	0	0	0	0
	OD132.6	3	19	20,34	32,4	91	60	66	68	70	71
	OD132.6	4	17	27,12	32,4	93	43	53	56	58	61
	OD132.6	5	15	33,9	32,4	94	30	43	46	49	52
	OD132.6	6	13	40,68	32,4	95	18	34	38	41	45
	OD132.6	7	12	47,46	32,4	95	7	25	29	34	38
	OD101.6	3	24	10,74	24,3	0	0	0	0	0	0
	OD101.6	4	20	14,32	24,3	0	0	0	0	0	0
	OD101.6	5	18	17,9	24,3	0	0	0	0	0	0
	OD101.6	6	16	21,48	24,3	0	0	0	0	0	0
	OD101.6	7	15	25,06	24,3	0	0	0	0	0	0
	OD101.6	8	14	28,64	24,3	0	0	0	0	0	0
	OD101.6	9	13	32,22	24,3	0	0	0	0	0	0
	OD101.6	10	13	35,8	24,3	0	0	0	0	0	0
	OD101.6	11	12	39,38	24,3	93	18	33	37	40	44
	OD101.6	12	11	42,96	24,3	94	12	28	32	36	40
	OD101.6	13	11	46,54	24,3	94	6	23	28	32	37

High Flux 26µ

Table C.4 – High Flux 26µ Ranking of core configurations.

						Score		Weight of Saturation			
Material	**Core ref.**	**Number of Cores**	**Number of Turns**	**Cross Section**	**Mag. Length**	**Saturation**	**Losses**	**0,2**	**0,25**	**0,3**	**0,35**
High Flux 26µ	OD165.1	1	25	9,87	41,2	74	92	88	87	86	85
	OD165.1	2	17	19,74	41,2	86	63	68	69	70	71
	OD165.1	3	13	29,61	41,2	91	35	46	49	52	54
	OD165.1	4	11	39,48	41,2	93	18	33	37	40	44
	OD165.1	5	10	49,35	41,2	94	1	20	24	29	34
	OD132.6	2	19	13,56	32,4	76	82	81	80	80	80
	OD132.6	3	15	20,34	32,4	83	63	67	68	69	70
	OD132.6	4	13	27,12	32,4	87	43	52	54	56	58
	OD132.6	5	11	33,9	32,4	90	28	41	44	47	50
	OD132.6	6	10	40,68	32,4	91	17	32	35	39	43
	OD132.6	7	9	47,46	32,4	93	6	23	27	32	36
	OD101.6	3	21	10,74	24,3	0	0	0	0	0	0
	OD101.6	4	17	14,32	24,3	0	0	0	0	0	0
	OD101.6	5	14	17,9	24,3	0	0	0	0	0	0
	OD101.6	6	13	21,48	24,3	0	0	0	0	0	0
	OD101.6	7	12	25,06	24,3	81	50	56	58	59	61
	OD101.6	8	11	28,64	24,3	84	39	48	51	53	55
	OD101.6	9	10	32,22	24,3	86	32	43	45	48	51
	OD101.6	10	10	35,8	24,3	86	26	38	41	44	47
	OD101.6	11	9	39,38	24,3	88	20	34	37	40	44
	OD101.6	12	9	42,96	24,3	88	14	29	32	36	40
	OD101.6	13	8	46,54	24,3	90	8	24	28	33	37

Kool Mu 26µ

Table C.5 – Kool Mu 26µ Ranking of core configurations.

						Score		Weight of Saturation			
Material	Core ref.	Number of Cores	Number of Turns	Cross Section	Mag. Length	Saturation	Losses	0,2	0,25	0,3	0,35
Kool Mu 26µ	OD165.1	1	37	9,87	41,2	0	0	0	0	0	0
	OD165.1	2	19	19,74	41,2	63	72	70	70	69	69
	OD165.1	3	15	29,61	41,2	72	89	86	85	84	83
	OD165.1	4	12	39,48	41,2	79	78	78	78	78	78
	OD165.1	5	11	49,35	41,2	81	66	69	70	70	71
	OD132.6	2	27	13,56	32,4	0	0	0	0	0	0
	OD132.6	3	18	20,34	32,4	54	64	62	61	61	60
	OD132.6	4	15	27,12	32,4	63	76	73	72	72	71
	OD132.6	5	13	33,9	32,4	68	76	74	74	73	73
	OD132.6	6	11	40,68	32,4	74	67	69	69	69	70
	OD132.6	7	10	47,46	32,4	77	59	62	63	64	65
	OD101.6	3	31	10,74	24,3	0	0	0	0	0	0
	OD101.6	4	26	14,32	24,3	0	0	0	0	0	0
	OD101.6	5	21	17,9	24,3	0	0	0	0	0	0
	OD101.6	6	17	21,48	24,3	0	0	0	0	0	0
	OD101.6	7	15	25,06	24,3	0	0	0	0	0	0
	OD101.6	8	13	28,64	24,3	0	0	0	0	0	0
	OD101.6	9	12	32,22	24,3	60	34	39	41	42	43
	OD101.6	10	11	35,8	24,3	63	30	37	38	40	42
	OD101.6	11	10	39,38	24,3	67	25	34	36	38	40
	OD101.6	12	10	42,96	24,3	67	21	30	32	35	37
	OD101.6	13	9	46,54	24,3	71	16	27	30	33	36

Appendix D

Winding design – Solid wire

In this section are presented the results for all the solid winding configurations taken into consideration.

D.1 – Solid Winding Results

Table D.1 – Solid winding design results.

diameter [mm]	A_{wire} [mm^2]	Parallel branches	Wire layers	J [A/mm^2]	R_{dc} [mΩ]	P_{dc} [W]	P_{ac} [W]	P_{wire} [W]	Copper Volume [cm^3]
5	19,6	5	3	3,1	0,791	71,2	25,8	97,0	428
5	19,6	4	2	3,8	0,949	85,4	11,9	97,3	329
4,75	17,7	6	3	2,8	0,741	66,7	23	89,7	471
4,75	17,7	5	3	3,4	0,855	77,0	26,5	103,5	377
4,75	17,7	4	2	4,2	1,033	93,0	12,3	105,3	292
4,5	15,9	7	3	2,7	0,709	63,8	20,8	84,6	493
4,5	15,9	6	3	3,1	0,803	72,3	23,6	95,9	411
4,5	15,9	5	3	3,8	0,925	83,2	27,2	110,4	329
4,5	15,9	4	2	4,7	1,129	101,6	12,8	114,4	257
4,25	14,2	7	3	3,0	0,773	69,5	21,4	90,9	428
4,25	14,2	6	3	3,5	0,876	78,8	24,3	103,1	356
4,25	14,2	5	2	4,2	1,016	91,4	10,8	102,2	287
4	12,6	8	3	3,0	0,758	68,2	19,8	88,0	430
4	12,6	7	3	3,4	0,847	76,2	22,1	98,3	368
4	12,6	6	3	4,0	0,958	86,3	25	111,3	306
4	12,6	5	2	4,8	1,124	101,2	11,3	112,5	249
3.5	9.6	10	4	3.1	0.78	70.1	34.2	104.3	405
3.5	9.6	9	3	3.5	0.85	76.2	19.3	95.5	357
3.5	9.6	8	3	3.9	0.94	84.2	21.4	105.6	311
3.5	9.6	7	3	4.5	1.04	93.9	23.8	117.7	266
3.5	9.6	6	2	5.2	1.19	107.5	24.1	131.6	224